Title

Intestinal transit amplifying cells require METTL3 for growth factor signaling, KRAS expression, and cell survival

Authors

Charles H. Danan[1,2,3], Kaitlyn E. Naughton[1], Katharina E. Hayer[4,5,6], Sangeevan Vellappan[7,8,9], Emily A. McMillan[1], Yusen Zhou[1,4], Rina Matsuda[3,10], Shaneice K. Nettleford[1], Kay Katada[1,3], Louis R. Parham[1,3], Xianghui Ma[1], Afrah Chowdhury[1], Benjamin J. Wilkins[6], Premal Shah[8,9], Matthew D. Weitzman[3,5,6], Kathryn E. Hamilton[1,3,11*]

Affiliations

[1]Division of Gastroenterology, Hepatology, and Nutrition; Department of Pediatrics; Children's Hospital of Philadelphia; Perelman School of Medicine, University of Pennsylvania, Philadelphia, PA, 19104, USA;
[2]Medical Scientist Training Program, Perelman School of Medicine, University of Pennsylvania, Philadelphia, PA, 19104, USA;
[3]Perelman School of Medicine, University of Pennsylvania, Philadelphia, PA, 19104, USA;
[4]Department of Biomedical and Health Informatics, The Children's Hospital of Philadelphia, Philadelphia, PA, 19104, USA
[5]Division of Protective Immunity, Children's Hospital of Philadelphia, Philadelphia, PA, 19104, USA;
[6]Department of Pathology and Laboratory Medicine, Perelman School of Medicine; University of Pennsylvania, Philadelphia, PA, 19104, USA;
[7]Waksman Institute of Microbiology, Rutgers University, Piscataway, NJ, 08854, USA;
[8]Department of Genetics, Rutgers University, Piscataway, NJ, 08854, USA;
[9]Human Genetics Institute of New Jersey, Piscataway, NJ, 08854, USA;
[10]Department of Pathobiology, School of Veterinary Medicine, University of Pennsylvania, Philadelphia, PA, 19104, USA;
[11]Institute for Regenerative Medicine, University of Pennsylvania, Philadelphia, PA, 19104, USA.

*Corresponding Author

Kathryn E. Hamilton, PhD
903 Abramson Research Building
Children's Hospital of Philadelphia
3615 Civic Center Blvd.
Philadelphia, PA 19104, USA
267-426-5266
hamiltonk1@chop.edu

Conflict-of-interest statement

Premal Shah is a member of the Scientific Advisory Board of Trestle Biosciences and is Director at Ananke Therapeutics. All other authors declare they have no competing interests.

Abstract

Intestinal epithelial transit amplifying cells are essential stem progenitors required for intestinal homeostasis, but their rapid proliferation renders them vulnerable to DNA damage from radiation and chemotherapy. Despite their critical roles in intestinal homeostasis and disease, few studies have described genes that are essential to transit amplifying cell function. We report that the RNA methyltransferase, METTL3, is required for survival of transit amplifying cells in the murine small intestine. Transit amplifying cell death after METTL3 deletion was associated with crypt and villus atrophy, loss of absorptive enterocytes, and uniform wasting and death in METTL3-depleted mice. Ribosome profiling and sequencing of methylated RNAs in enteroids and *in vivo* demonstrated decreased translation of hundreds of unique methylated transcripts after METTL3 deletion, particularly transcripts involved in growth factor signal transduction such as *Kras*. Further investigation confirmed a novel relationship between METTL3 and *Kras* methylation and protein levels *in vivo*. Our study identifies METTL3 as an essential factor supporting the homeostasis of small intestinal tissue via direct maintenance of transit amplifying cell survival. We highlight the crucial role of RNA modifications in regulating growth factor signaling in the intestine, with important implications for both homeostatic tissue renewal and epithelial regeneration.

MAIN TEXT

Introduction

The intestinal epithelium digests and absorbs nutrients, protects against pathogen invasion, and regulates interactions between mucosal immune cells and the gut lumen (1). These essential functions are made possible by the continuous renewal of differentiated intestinal epithelial cells (2). Epithelial renewal begins at the intestinal crypt base, where intestinal stem cells expressing the Wnt target gene, LGR5, initiate differentiation and migrate up the crypt wall. As they move up the crypt wall, LGR5+ stem cells differentiate into intestinal stem progenitors known as transit amplifying (TA) cells (2). TA cells rapidly undergo successive cycles of proliferation to generate the bulk of intestinal epithelium. While existing research emphasizes the role of LGR5+ stem cells in tissue renewal, TA cells are the primary site of intestinal

epithelial proliferation and differentiation, and they produce the majority of differentiated epithelium (3, 4). Rapid proliferation is the central defining feature of TA cells, and it renders them particularly vulnerable to DNA damaging agents such as chemotherapeutics and radiation therapy (5–7). These routine cancer treatments cause chemotherapy-induced gastrointestinal toxicity (CIGT) and radiation induced gastrointestinal syndrome (GIS). CIGT and GIS together affect >80% of cancer patients. They are debilitating pathologies with limited treatment options (8–10). One potential therapeutic avenue would be the development of drugs that protect the TA cells preferentially damaged by these common cancer therapies. However, despite their critical roles in intestinal homeostasis and disease, factors that maintain survival and proliferation of TA cells remain inadequately defined compared to the extensive study of LGR5+ stem cells.

Novel approaches are needed to identify factors that specifically regulate TA cell function. While numerous studies have defined transcriptional control of intestinal stem cells, post-transcriptional regulation of intestinal epithelial homeostasis is only beginning to be understood. Recent research points to important roles for the RNA modification, N6-methyladenosine (m^6A), in intestinal crypts (11–15). N6-methyladenosine is the most common covalent modification of RNA, occurring on approximately 25% of mRNA transcripts (16, 17). It acts by recruiting RNA-binding proteins that affect mRNA fate, predominantly stability and translation. (18). Global m^6A methylation patterns in the epithelium can shift with microbial and nutrient contents of the gut and m^6A-binding proteins have been implicated in intestinal regeneration and the pathogenesis of inflammatory bowel disease (IBD) (11, 13, 15, 19, 20). These studies suggest critical roles for m^6A in integrating environmental cues with homeostatic and regenerative processes in the intestinal epithelium.

Despite advances in the study of m^6A in the gut, the effect of global depletion of m^6A in the intestinal epithelium remains unclear and contradictory. A highly conserved m^6A “writer” complex installs m^6A co-transcriptionally in the nucleus of eukaryotic cells. At the core of this complex are the writer proteins Methyltransferase-like 3 and 14 (METTL3 and METTL14) (18). Although METTL3 is the catalytic subunit, both METTL3 and METTL14 are thought to be essential for the methylating activity of the complex (21, 22), and both METTL proteins are deleted interchangeably to define the role of m^6A in specific tissue or cell types. Recent studies reported essential functions for METTL14 in the survival of LGR5+ stem cells in the

colon, but not the small intestine (23, 24). In contrast, another study found that METTL3 deletion caused defects in LGR5+ stem cells in the small intestine (25). However, in the case of METTL3 deletion, rescue of LGR5+ stem cell survival could not rescue tissue homeostasis. Therefore, the primary defect in METTL3-depleted epithelium remains unclear.

In contrast to previous reports emphasizing dysfunction of LGR5+ stem cells, we found that METTL3 deletion induced profound cell death predominantly in small intestinal transit amplifying cells. Disruption of the TA zone was associated with crypt and villus atrophy and widespread reduction in absorptive enterocytes, ultimately resulting in the death of METTL3-depleted mice. Sequencing of m^6A-modified RNA *in vivo* and ribosome profiling in METTL3-depleted enteroids revealed decreased translation efficiency of methylated transcripts critical to growth factor signaling, including master growth regulator and proto-oncogene, *Kras*. Additional investigation confirmed a novel link between METTL3 and *Kras* methylation and protein expression. Our data identify METTL3 as an essential regulator of intestinal transit amplifying cell survival via direct support of growth factor signaling and KRAS expression. By identifying epitranscriptomic regulation as an indispensable process within TA cells, we highlight a novel gene regulatory mechanism in this critical but poorly understood cell type.

Results

Intestinal epithelial METTL3 deletion results in complete growth failure and mortality

To determine the role of METTL3 in intestinal epithelial development and homeostasis, we paired *Mettl3*$^{flox/flox}$ mice with the pan-intestinal-epithelial *Villin*-Cre (*Mettl3*$^{VilCre\Delta/\Delta}$) or its tamoxifen inducible counterpart, *Villin-CreERT2* (inducible *Mettl3*$^{VilCreER\Delta/\Delta}$). First, we examined *Mettl3*$^{VilCre\Delta/\Delta}$ mice, which had constitutive Cre activation in the small intestinal and colonic epithelium beginning at embryonic day 12.5 (26). These mice were born with Mendelian distribution (X^2 n=79 p>0.85) and appeared grossly normal at postnatal day 14, as previously described (27). However, from postnatal day 21 to 28, *Mettl3*$^{VilCre\Delta/\Delta}$ mice lost ~20% starting body weight while controls gained ~40% (Figure 1A). Body condition and weight loss in

126 *Mettl3*$^{VilCre\Delta/\Delta}$ mice required euthanasia of 70% of mice between postnatal day 16-29 (Figure 1, B-D). To
127 determine whether this phenotype was development-specific, we next examined inducible *Mettl3*$^{VilCreER\Delta/\Delta}$
128 mice injected with tamoxifen at 8 weeks of age (Figure 2A). After their final tamoxifen injection, inducible
129 *Mettl3*$^{VilCreER\Delta/\Delta}$ mice exhibited an average daily weight loss of ~2.5% (Figure 2B). Within 10 days, almost
130 all mice experienced critical (>20%) weight loss requiring euthanasia (Figure 2, B and C). These data
131 demonstrate a requirement of METTL3 for growth and survival during the postnatal period and adulthood.
132
133 **METTL3 deletion induces small intestinal crypt and villus atrophy**
134
135 We next examined the intestinal pathology of *Mettl3*$^{VilCre\Delta/\Delta}$ and inducible *Mettl3*$^{VilCreER\Delta/\Delta}$ mice to
136 determine the cause of their severe growth failure and mortality. Western blot, *in situ* staining, and m^{6}A dot
137 blot confirmed depletion of METTL3 and m^{6}A in the intestinal epithelium (Supplemental Figure 1, A-C, and
138 Supplemental Figure 2, A and B). Using a composite histopathological score in both METTL3 knockout
139 models, we noted severe small intestinal defects defined by widespread crypt atrophy alongside villus
140 shortening (Figure 1, E-G, and Figure 2, D-F). We also noted occasional hypertrophic regenerative crypts
141 (Figure 1E and Figure 2D). Although defects were most severe in the distal small intestine, we observed
142 histological changes from the proximal small intestine to the proximal colon. The distal colon was relatively
143 spared (Figure 1, H and I, and Figure 2, G-I). Since METTL3 and METTL14 knockouts are generally
144 considered equivalent, our findings were striking and unexpected given previous studies indicating
145 METTL14 deletion induces severe distal colonic defects but spares the small intestine (23, 24). These data
146 demonstrate that intestinal epithelial METTL3 is required for both the postnatal development and adult
147 maintenance of full-length crypt and villus structures, particularly in the distal small intestine.
148
149 **METTL3 is required for intestinal epithelial proliferation and survival**
150
151 To determine the origins of crypt and villus atrophy, we next evaluated proliferation and apoptosis
152 in *Mettl3*$^{VilCre\Delta/\Delta}$ and inducible *Mettl3*$^{VilCreER\Delta/\Delta}$ mice. Since histological changes were most severe in the distal
153 small intestine, we focused on Ki67 and TUNEL staining in this tissue. In METTL3 knockout epithelium,

154 atrophied crypts previously observed by H&E exhibited drastically reduced Ki67 staining. Where control
155 crypts had an average of ~30 Ki67+ cells/crypt, METTL3 depleted crypts often exhibited fewer than 10
156 Ki67+ cells (Figure 1, J and K, and Figure 2, N and O). We also observed some hyperproliferative crypts in
157 both deletion models (>45 Ki67+ cells), although in inducible *Mettl3*$^{VilCreER\Delta/\Delta}$ mice, these were frequently
158 METTL3+ by immunofluorescence (Supplemental Figure 2C). We also identified a >10-fold increase in the
159 mean number of TUNEL positive cells in both *Mettl3*$^{VilCre\Delta/\Delta}$ and inducible *Mettl3*$^{VilCreER\Delta/\Delta}$ mice,
160 demonstrating extensive cell death throughout the villus and crypt (Figure 1L and Figure 2P). These data
161 suggest that both disrupted proliferation and cell survival contributed to epithelial defects in *Mettl3*$^{VilCre\Delta/\Delta}$
162 and inducible *Mettl3*$^{VilCreER\Delta/\Delta}$ mice.
163
164 **METTL3 is required for absorptive enterocyte maturation**
165
166 To evaluate etiologies of weight loss and epithelial distortion in METTL3 knockout mice, we
167 examined the distribution of differentiated epithelial cells. The differentiated intestinal epithelium comprises
168 secretory and absorptive lineages, which both play essential roles in intestinal homeostasis. Secretory cell
169 depletion can promote epithelial defects due to important roles in producing mucus, antimicrobial
170 compounds, and stem cell niche factors (28, 29). However, even in areas of severe epithelial distortion, we
171 observed maintenance of MUC2+ goblet cells with only minor, inconsistent reductions in LYZ+ Paneth cells
172 and CHGA+ enteroendocrine cells (Figure 1, M-O, and Figure 2, J-L). Alcian blue staining corroborated
173 these findings by indicating mucus production was also maintained in the small intestine, though we did
174 observe reductions in mucus in the proximal colon (Supplemental Figures 1D and 2D). In contrast to modest
175 changes in secretory lineages, we observed a ~50% decrease in alkaline phosphatase staining in the distal
176 small intestine of both *Mettl3*$^{VilCre\Delta/\Delta}$ mice and inducible *Mettl3*$^{VilCreER\Delta/\Delta}$ mice compared to controls,
177 suggesting dramatic loss of absorptive enterocytes (Figure 1P and Figure 2M). This effect was strongest in
178 areas of severe villus shortening, where we observed almost no alkaline phosphatase staining. Taken
179 together, we find general maintenance of secretory cells but a dramatic reduction in mature absorptive
180 enterocytes in *Mettl3*$^{VilCre\Delta/\Delta}$ mice and inducible *Mettl3*$^{VilCreER\Delta/\Delta}$ mice. We propose that the resulting loss of
181 absorptive capacity may underlie wasting in these knockout mice.

182

183 **Alternative METTL3 deletion recapitulates small intestinal defects**

184

185 We performed the above experiments in inducible *Mettl3*$^{VilCreER\Delta/\Delta}$ mice using *loxP* sites spanning
186 nine exons of the *Mettl3* locus (Supplemental Figure 3A) (30). This large deletion resulted in some reduction
187 of recombination efficiency in the distal colon and to a lesser degree, the small intestine (Supplemental
188 Figure 2, B and C). We were also surprised to identify a small intestinal defect after METTL3 deletion
189 because previously described METTL14 deletion produces no small intestinal phenotype (23, 24). To
190 address these concerns, we tested a second METTL3 deletion model with *LoxP* sites spanning only exon
191 4 (*Mettl3*$^{VilCreER\Delta 2/\Delta 2}$, Supplemental Figure 3B) (31). Inducible *Mettl3*$^{VilCreER\Delta 2/\Delta 2}$ mice demonstrated efficient
192 deletion of METTL3 in all targeted tissues (Supplemental Figure 3C). In this additional model, we confirmed
193 rapid weight loss and mortality, hypo- and hyper-plastic crypts, preservation of secretory goblet and Paneth
194 cells, and absent distal colonic defects (Supplemental Figure 3, D to G). These data further support the
195 conclusion that METTL3 is essential for small intestinal homeostasis.

196

197 **Intestinal defects with METTL3 deletion are independent of intestinal microbiota**

198

199 Microbial translocation and inflammatory activation are common causes of morbidity and mortality
200 in mice with intestinal epithelial defects. We therefore examined sera of inducible *Mettl3*$^{VilCreER\Delta/\Delta}$ mice for
201 elevated inflammatory cytokines. Intriguingly, there was no significant difference in serum cytokine markers
202 TNF-α, IL-6, IL-1α, IL-1β, IL-10, IL-12 or IFN-γ in *Mettl3*$^{VilCreER\Delta/\Delta}$ mice compared to controls (Figure 3A).
203 Additionally, spleen size—often positively correlated with degree of whole-body inflammation—was
204 reduced (Figure 3B), and small intestine and colon lengths—often reduced in inflammatory conditions—
205 were unchanged (Figure 3, C and D). Taken together, these data suggested a non-inflammatory etiology
206 to morbidity and mortality in *Mettl3*$^{VilCreER\Delta/\Delta}$ mice.

207 Despite no overt inflammatory pathology, the contribution of facility-specific microbiota is a common
208 concern in the evaluation of intestinal phenotypes. We also questioned whether the microbiota contributed
209 to the surprising difference in small intestinal phenotypes between METTL3 and previously described

210 METTL14 knockout intestinal epithelium (23, 24). Therefore, we depleted the microbiota in *Mettl3*$^{VilCreER\Delta/\Delta}$
211 mice by adding an antibiotic cocktail to their drinking water beginning one week before tamoxifen injection
212 (Figure 3E). Quantitative PCR of genomic 16s rRNA confirmed ~1000-fold depletion of luminal bacteria
213 (Figure 3F). There was no change in weight loss or mortality in microbiota depleted *Mettl3*$^{VilCreER\Delta/\Delta}$ mice
214 compared to those on normal drinking water (Figure 3, G and H). Histological abnormalities also persisted
215 in microbiota depleted *Mettl3*$^{VilCreER\Delta/\Delta}$ mice (Figure 3I). Taken together, these data suggest minimal
216 contribution of inflammation or microbiota to the gross and histological defects seen in *Mettl3*$^{VilCreER\Delta/\Delta}$ mice.
217 Rather, they further support a model in which loss of absorptive enterocytes diminishes digestive capacity
218 leading to weight loss and mortality in these mice.
219
220 **METTL3 deletion immediately triggers transit amplifying cell death**
221
222 Inducible *Mettl3*$^{VilCreER\Delta/\Delta}$ mice displayed a complex set of histological phenotypes, including
223 adjacent hypertrophic and atrophic crypts and scattered villus and crypt cell death. Some of these changes
224 may be reactive, secondary changes rather than immediately downstream of METTL3 depletion. We
225 therefore examined inducible *Mettl3*$^{VilCreER\Delta/\Delta}$ mice two days after the final tamoxifen injection- the earliest
226 timepoint at which we confirmed METTL3 deletion by immunoblot and *in situ* staining (Figure 4A and
227 Supplemental Figure 2, A and B). At this early deletion timepoint, *Mettl3*$^{VilCreER\Delta/\Delta}$ mice demonstrated a ~30%
228 increase in crypt height in the small intestine (Figure 4B). This change was associated with increased
229 numbers of Ki67+ cells (Figure 4C) and increased expression of transcripts associated with stem cells and
230 stem progenitors, including key stem cell marker *Lgr5* (Figure 4D). In contrast, we observed profound TA
231 cell death in inducible *Mettl3*$^{VilCreER\Delta/\Delta}$ mice at this same early timepoint. The mean number of TUNEL+ foci
232 per crypt was elevated >20-fold in *Mettl3*$^{VilCreER\Delta/\Delta}$ crypts compared to controls (Figure 4E). Strikingly, almost
233 all TUNEL+ foci in *Mettl3*$^{VilCreER\Delta/\Delta}$ small intestine were in the TA zone, located between the crypt base and
234 the crypt-villus junction. We quantified TUNEL+ staining in the crypt base, TA zone, and villus epithelium
235 and found 3-fold higher cell death rates in the TA zone compared to the crypt base (Figure 4F). These data
236 suggest that the initial defect in inducible *Mettl3*$^{VilCreER\Delta/\Delta}$ mice is widespread transit amplifying cell death.
237

238 **METTL3 deletion causes growth arrest and death in intestinal enteroids**

239

240 We next wanted to establish an epithelial-specific model for examining the kinetics and mechanism
241 of cell death in *Mettl3*$^{VilCreER\Delta/\Delta}$ mice. We therefore generated 3D organoids from small intestinal crypts
242 (enteroids) and colonic crypts (colonoids) of *Mettl3*$^{VilCreER\Delta/\Delta}$ and *Mettl3*$^{flox/flox}$ mice and treated with 4-
243 hydroxytamoxifen (4-OHT) *in vitro* to induce METTL3 deletion (32). We first monitored gross cell death in
244 enteroids and colonoids. We defined dead organoids as those with a complete opaque appearance, leaking
245 of dead cell debris, and absent growth over the subsequent 24 hours. Nearly all *Mettl3*$^{VilCreER\Delta/\Delta}$ enteroids
246 and proximal colonoids died within 5 days post 4-OHT withdrawal (Figure 5, B and C). Only distal colonoids
247 from *Mettl3*$^{VilCreER\Delta/\Delta}$ mice survived 4-OHT treatment, where immunoblotting confirmed deletion of METTL3
248 (Figure 5D). To map the chronology of enteroid growth and survival after METTL3 deletion, we measured
249 ileal enteroid size and death daily after 4-OHT treatment of *Mettl3*$^{VilCreER\Delta/\Delta}$ and control *Villin-CreERT2*
250 enteroids. Enteroids appeared grossly normal in the first two days after 4-OHT withdrawal. At day 3,
251 *Mettl3*$^{VilCreER\Delta/\Delta}$ enteroids exhibited growth arrest concurrent with increased death, ultimately resulting in
252 complete death by five days post 4-OHT (Figure 5, E-G). In summary, *Mettl3*$^{VilCreER\Delta/\Delta}$ enteroids and
253 colonoids recapitulated tissue-region-specific cell death phenotypes observed *in vivo*. These data
254 confirmed that cell death phenotypes after METTL3 deletion were epithelial-cell-autonomous; they also
255 established enteroids as an effective model of *in vivo* pathologies for further mechanistic investigation.

256

257 **Catalytic inactive METTL3 does not rescue death of METTL3 depleted enteroids**

258

259 Given that METTL3 deletion led to small intestinal epithelial death *in vivo* and *in vitro*, but depletion
260 of the essential methyltransferase co-factor METTL14 has been previously reported to have no effect on
261 small intestinal homeostasis (23, 24), we hypothesized that METTL3 might support intestinal epithelial
262 survival through a non-catalytic mechanism. We reintroduced a non-catalytic METTL3 (DPPW$^{395\text{-}398}$ to
263 APPA$^{395\text{-}398}$) (33) to *Mettl3*$^{VilCreER\Delta/\Delta}$ ileal enteroids using a lentiviral construct (METTL3$^{\Delta cat}$). Western and
264 dot blot confirmed rescue of METTL3 expression and depletion of m^{6}A in these enteroids (Supplemental
265 Figure 4, A and B). Compared to *Mettl3*$^{VilCreER\Delta/\Delta}$, *Mettl3*$^{VilCreER\Delta/\Delta}$ + METTL3$^{\Delta cat}$ enteroids demonstrated

266 delayed cell death through the 4th day post 4-OHT, but still died by day 5 and did not survive to subsequent
267 passages (Supplemental Figure 4, C-E). Previous reports indicated that METTL3 may act independently of
268 METTL14 as a non-catalytic cytoplasmic regulator of protein translation (34–36). However, we observed
269 exclusively nuclear staining of endogenous METTL3 in ileal enteroids, likely precluding this possibility
270 (Supplemental Figure 4F). These data suggest that small intestinal epithelium requires the nuclear, catalytic
271 activity of METTL3 for homeostatic function.
272
273 **METTL3 deletion triggers global downregulation of translational efficiency**
274
275 Previous studies indicate that m^6A induces global changes in mRNA abundance and translational
276 efficiency (13, 37, 38). To identify METTL3 targets that may mediate phenotypes observed *in vivo* and *in*
277 *vitro*, we sequenced total RNA and ribosome-protected RNA fragments to assay global changes in RNA
278 abundance and translation after METTL3 deletion. Since METTL3 modifies thousands of transcripts with
279 pleiotropic effects, we elected to analyze *Mettl3*$^{VilCreER\Delta/\Delta}$ ileal enteroids 72 hours after 4-OHT treatment to
280 detect the changes most proximal to METTL3 deletion but prior to widespread cell death. Comparing the
281 approximately 25,000 transcripts detected in both data sets, METTL3 deletion impacted more transcripts
282 at the level of RNA translation than abundance. We found 6,101 transcripts exclusively altered at the level
283 of ribosome protected fragments, 3,004 with changes only in RNA abundance, and 1,374 with changes in
284 both (Figure 6A and Data S1). We next compared the ratio of ribosome protected fragments to mRNA
285 abundance for each transcript to generate the translational efficiency ("TE") of each transcript (11, 39).
286 Averaging all 2,124 transcripts with significant changes in TE, the predominant effect of METTL3 deletion
287 was reduced TE, with 1,747 transcripts exhibiting reduced TE and 377 with increased TE. Taken together,
288 there was a mean decrease in TE of 39% across all differentially translated transcripts in *Mettl3*$^{VilCreER\Delta/\Delta}$
289 enteroids compared to controls (Figure 6B). These data suggest a novel role for METTL3 in broadly
290 supporting translation in the small intestinal epithelium.
291
292 **METTL3 deletion downregulates translation of methylated transcripts regulating growth factor**
293 **signaling**

294

295 We next performed m^{6}A immunoprecipitation and sequencing (m^{6}A-seq) in wildtype mouse crypts
296 *in vivo* to define putative direct targets of METTL3 (16, 17, 40). m^{6}A-seq yielded 13,763 m^{6}A peaks within
297 7,882 unique transcripts (Data S2). Peaks were distributed across the coding sequence and 3' untranslated
298 region, with the highest accumulation at the stop codon, consistent with previous reports (Supplemental
299 Figure 5A) (16, 17). We also saw expected patterns of m^{6}A enrichment in positive and negative control
300 transcripts (Supplemental Figure 5B). We superimposed m^{6}A-seq data onto ribosome profiling data and
301 found that of the 1,747 transcripts with decreased TE after METTL3 deletion, 363 transcripts contained at
302 least one m^{6}A peak (Figure 6, C and D). We conducted pathway enrichment analysis on these 363
303 transcripts using Gene Ontology Biological Process (GOBP) gene sets. We observed the most significant
304 enrichment in transcripts associated with growth factor signaling cascades (Figure 6E). Amongst these
305 transcripts, the largest magnitude reduction in mean TE was for *Kras*, an essential intestinal proto-
306 oncogene that promotes intestinal epithelial proliferation and survival (Figure 6F) (41). Taken together, our
307 ribosome profiling and m^{6}A-seq data indicate that METTL3 deletion downregulates translation of
308 methylated transcripts supporting growth factor signaling, including *Kras*.

309

310 **METTL3 deletion reduces *Kras* methylation and protein levels and induces cellular senescence**

311

312 We further explored the putative relationship between METTL3 and KRAS expression by examining
313 m^{6}A modification of the *Kras* transcript. Our m^{6}A-seq data indicated enriched m^{6}A density across the *Kras*
314 gene body, including both UTRs (Figure 7A). To verify m^{6}A-seq peaks on the *Kras* transcript and determine
315 their dependence on METTL3 expression, we performed m^{6}A-RNA-immunoprecipitation-qPCR (m^{6}A-RIP-
316 qPCR) in crypt-enriched lysates from *Mettl3$^{flox/flox}$* and *Mettl3$^{VilCreER\Delta/\Delta}$* mice three days after final tamoxifen
317 injection. Using qPCR probes targeting both the *Kras* 5' and 3' UTR we found significant enrichment of both
318 transcript regions in m^{6}A-RIP fractions. However, only m^{6}A enrichment in the 3' UTR appeared dependent
319 on METTL3 expression. The 5' UTR peak may represent N6,2′-O-dimethyladenosine (m^{6}Am), a terminal
320 modification added to the mRNA cap by the methyltransferase PCIF1; m^{6}Am is an established off-target of

321 m^{6}A antibodies (Figure 7, B and C) (42). These data support the novel finding that METTL3 methylates
322 *Kras* at the 3'UTR.

323 We next examined how methylation of *Kras* impacts its expression *in vivo*. Although METTL3
324 deletion did not significantly impact *Kras* transcript abundance via qPCR, we observed a decrease in KRAS
325 protein in crypt-enriched lysates from *Mettl3*$^{VilCreER\Delta/\Delta}$ mice compared to controls (Figure 7, D and E). To
326 further validate our Ribo-seq data *in vivo*, we also examined protein expression levels of other top
327 downregulated genes of interest. We confirmed decreases in YES1 (src family kinase and proto-oncogene)
328 and SEC13 (member of the nuclear pore complex implicated in mRNA export) but not UBE1 (primary
329 enzyme in conjugation of ubiquitin) (43–45) (Figure 7E). Taken together, these data suggest that METTL3
330 promotes KRAS expression without impacting *Kras* transcript levels, providing further mechanistic support
331 for METTL3 as a post-transcriptional regulator of *Kras*.

332 KRAS is a key mediator of epidermal growth factor (EGF) signaling in epithelial cells (41). Loss of
333 mitogenic signals such as EGF induces cell cycle arrest and senescence in proliferative cells (46). EGF
334 signaling has also been implicated in maintaining genomic integrity in hematopoietic stem cells (47). We
335 therefore assessed senescence and double-stranded DNA breaks in inducible *Mettl3*$^{VilCreER\Delta/\Delta}$ epithelium
336 by staining for p21 and γ-H2AX two days after final tamoxifen injection. *Mettl3*$^{VilCreER\Delta/\Delta}$ crypts demonstrated
337 elevated p21 and γ-H2AX compared to controls, particularly in the TA zone (Figure 7F and 7G). One
338 potential caveat to this finding is the possibility of toxic combined effects of CreERT2 and tamoxifen in
339 intestinal stem cells within a week of tamoxifen exposure (48). To address this, we evaluated p21 and γ-
340 H2AX in tamoxifen-treated *Villin-CreERT2* control mice at the same timepoint. Both p21 and γ-H2AX were
341 significantly increased in *Mettl3*$^{VilCreER\Delta/\Delta}$ mice compared to *Villin-CreERT2* controls (Supplemental Figure
342 6, A and B). Taken together, these data support the hypothesis that loss of growth factor and KRAS
343 signaling after METTL3 deletion triggers cellular senescence and DNA damage in the crypt TA zone.
344

345 ## Discussion

346

347 Our collective findings examining METTL3 deletion in the intestinal epithelium *in vivo* and *in vitro*
348 support a model in which METTL3 methylates the *Kras* transcript and other transcripts involved in growth
349 factor signal transduction. Methylation promotes translation of these transcripts, maintaining
350 responsiveness to extracellular growth factors and thus maintaining proliferation and survival in the transit
351 amplifying cells of the crypt. In the absence of METTL3, loss of growth factor pathway members such as
352 KRAS leads to cellular senescence and genomic instability. Pathological effects of METTL3 deletion
353 manifest strongest in the TA zone because rapid proliferation demands the expression of proteins involved
354 in transducing growth factor signals. Ultimately, loss of transit amplification reduces crypt and villus size
355 and diminishes absorptive cell maturation without impacting secretory cells (Figure 8).

356 We originally expected that METTL3 deletion would have no overt effect on the small intestinal
357 epithelium because previous reports showed that METTL14 was dispensable in the small intestine (23,
358 24). While our study does not directly compare METTL3 and METTL14, discrepancies between the
359 present study and previously described METTL14 knockout studies could be due to facility-specific
360 differences (e.g., microbiota). Several factors minimize this possibility. First, two independent groups from
361 the US and China reported colonic but not small intestinal phenotypes with METTL14 knockout,
362 demonstrating persistent phenotypes across mouse facilities. Furthermore, we found small intestinal
363 phenotypes followed METTL3 deletion when testing both constitutive and inducible Cre-drivers, two
364 *Mettl3-floxed* lines, microbiota-depleted mice, and mouse-derived enteroids. The consistency of small
365 intestinal phenotypes spanning numerous orthogonal modes of METTL3 deletion strongly suggests that
366 METTL3 and METTL14 act independently in the small intestine. This unexpected finding suggests novel
367 divergent roles for METTL3 and METTL14 in the gut and underscores the value of examining m^6A writer
368 proteins in their native context.

369 Despite their critical role in maintaining homeostatic renewal of the intestinal epithelium, transit
370 amplifying cell dynamics remain poorly understood. We propose that METTL3 is essential for both
371 differentiation and renewal in the transit amplifying zone of the small intestinal crypt. As the site of stem
372 progenitor differentiation, transit amplifying cells are critical to the process of lineage commitment in the

373 cell (2). We observed general maintenance of secretory cells adjacent to areas of atrophic crypts in
374 *Mettl3*^{VilCre} and *Mettl3*$^{VilCreER\Delta/\Delta}$ mice. In contrast, these histologically affected areas demonstrated little to
375 no absorptive cell staining. Since mature absorptive cells make up most of the villus surface, transit
376 amplification in the crypt is essential for the production of adequate numbers of absorptive progenitors
377 rather than secretory cells (49). Consistent with our data showing decreased enterocyte maturation
378 concurrent with loss of transit amplifying cells, a recent study suggested a causal relationship between
379 decreased TA proliferation and an increase in the ratio of secretory to absorptive cells (4). Therefore, we
380 propose that METTL3 promotes the production of absorptive cells by maintaining TA cell proliferation.
381 Inducible METTL3 deletion was also associated with a >20-fold increase in the rate of cell death
382 in the small intestinal crypt, especially in cells of the TA zone. TA cell death immediately followed deletion
383 of METTL3, exceeded rates of cell death in the crypt base 3-fold, and occurred at a timepoint when
384 markers of crypt base stem cells (*e.g., Lgr5*) were preserved or even increased. Therefore, we conclude
385 that the primary, initiating defect in METTL3 depleted epithelium is the death of transit amplifying cells. A
386 recent study posited that TA cells regulate the proliferation of LGR5+ stem cells by controlling the
387 secretion of R-spondins (50). Thus, an initial defect in the TA zone could precipitate the loss of LGR5+
388 stem cells observed by other groups (25). We also noted increased crypt proliferation at this time of
389 profound proliferative cell death, which initially seemed paradoxical. However, we hypothesize that this
390 increased proliferation represents a regenerative response to increased cell death. Ultimately, the
391 extreme rate of TA cell death appeared to overcome this hyperproliferative response, since most affected
392 crypts exhibited severely diminished proliferation 1-2 weeks after initiating METTL3 deletion. Thus, we
393 conclude that METTL3 specifically regulates the survival of intestinal transit amplifying cells.
394 Rapid proliferation in the TA zone suggests enhanced dependence on mitogenic factors in these
395 cells. Consistent with this hypothesis, METTL3 deletion downregulated translation of multiple methylated
396 transcripts involved in growth factor signaling, including: growth factor receptor *Fgfr4* (51), src family
397 kinase *Yes1* (43), guanine nucleotide exchange factor *Tiam1* (52), and *Kras*. KRAS is a target of
398 particular interest due to its role as an oncogene in the gut (41), where up to 50% of colorectal cancers
399 harbor a KRAS mutation (53). KRAS binds to guanosine 5'-triphosphate (GTP) in response to
400 extracellular signals such as epidermal growth factor receptor (EGFR) activation. Activated KRAS-GTP

401 then upregulates growth factor targets such as PI3K-Akt, RAF-MEK-ERK, and the GLUT1 glucose
402 transporter (41). Although frequently dysregulated in cancer, these pathways are also essential for
403 homeostatic proliferation, differentiation, and survival (54). Our data support a novel direct relationship
404 between METTL3, *Kras* m^6A-methylation, and KRAS protein levels. We posit that widescale depletion of
405 growth factor signaling—including but not limited to KRAS—overwhelms cells of the TA zone and leads to
406 cell death with METTL3 deletion.

407 In summary, we identify METTL3 as an essential post-transcriptional regulator of growth factor
408 signaling and TA cell survival. Our work defines a novel mode of epi-transcriptomic gene regulation in this
409 critical but understudied cell type. This paves the way for future investigation of therapeutic targets that
410 preserve TA cells in the face of DNA damaging agents such as chemotherapeutics and irradiation.

411

412 ## Materials and Methods

413

414 **Animals**

415 *Mettl3*$^{VilCre\Delta/\Delta}$ and *Mettl3*$^{VilCreER\Delta/\Delta}$ were generated by crossing *Vil-Cre 1000* mice (JAX #021504) or *Villin-*
416 *CreERT2* mice (JAX #020282) to previously described *Mettl3*$^{flox/flox}$ mice (30) kindly provided by Dr.
417 Richard Flavell (Yale). *Mettl3*$^{VilCreER\Delta2/\Delta2}$ were generated by crossing *Villin-CreERT2* mice to previously
418 described *Mettl3*$^{flox2/flox2}$ mice (31), kindly provided by Dr. Federica Accornero (Ohio State). For the m^6A-
419 seq experiment, wildtype mice were used (JAX #000664). All mice were C57BL/6J strain and both male
420 and female mice were used. Mice were housed in a temperature-controlled room with 12-hour light and
421 dark cycles and continuous access to food and water.

422

423 **Tamoxifen injection, euthanasia criteria, and survival curves**

424 Mice aged 8-9 weeks were injected four times with 50 mg/kg tamoxifen at 10 mg/mL in corn oil at 24-hour
425 intervals. Mice were euthanized once they had reached humane endpoints defined by the IACUC
426 protocol, including: >20% body weight loss, hunched posture, emaciated body condition, or non-
427 responsiveness to stimuli. Survival curves were determined by the number of mice reaching a humane
428 endpoint on each day after tamoxifen injection.

429

430 **Microbial depletion**

431 *Mettl3*$^{flox/flox}$ and *Mettl3*$^{VilCreERΔ/Δ}$ mice were moved to new cages at 7 weeks of age and given sterile DI
432 water supplemented with 0.5g/L Ampicillin (Sigma A9518), 0.5g/L Neomycin (MP Biomedicals 180610),
433 0.5g/L Gentamicin (Sigma G1914-5G), 0.25g/L Vancomycin (VWR 0990), 0.25g/L Metronidazole (Thermo
434 210340050), and 4g/L Splenda to enhance taste. After seven days, mice were injected with tamoxifen for
435 four days as described above and stool collected on the final day of injection. Stool from *Mettl3*$^{flox/flox}$ and
436 *Mettl3*$^{VilCreERΔ/Δ}$ mice on normal drinking water was used as controls. DNA was extracted from stool using
437 the QIAamp Fast DNA Stool Mini Kit (Qiagen 51604) and quantitative PCR was performed as described
438 in the qPCR methods section using primer Ba04230899_s1. qPCR quantification was normalized to stool
439 weight.

440

441 **Serum cytokine quantification**

442 Serum supernatant was isolated from the inferior vena cava of euthanized mice and cytokines measured
443 using the Cytometric Bead Array (BD Biosciences) with the amount of capture beads, detection reagents,
444 and sample volumes scaled down tenfold from manufacturer's protocol. Data was collected on an
445 LSRFortessa flow cytometer (BD Biosciences) with FACSDiva v9.0 (BD Biosciences) and analyzed with
446 FlowJo v10 (BD Biosciences). Statistical outliers were removed in GraphPad Prism v9.3 using ROUT
447 method (Q=1%). Cytokine used were mouse TNFα (BD 558299), mouse IL-6 (BD 558301), mouse IL-1α
448 (BD 560157), mouse IL-1β (BD 560232), mouse IL-10 (BD 558300), mouse IL-12/IL-23p40 (BD 560151),
449 and mouse IFN-γ (BD 558296) with Mouse/Rat Soluble Protein Master Buffer Kit (BD 558266).

450

451 **Histology and immunofluorescent staining**

452 Intestines were Swiss-rolled and fixed overnight in 4% paraformaldehyde at 4˚C prior to processing and
453 embedding. Sections were blocked with Blocking Buffer (1% BSA and 10% donkey serum in PBS) for 1
454 hour, 25˚C, before staining with primary antibodies (Supplemental Table 1) at 1:200 overnight at 4˚C
455 followed by washing with PBS and staining with secondary antibodies at 25˚C for 25 minutes. Finally,
456 nuclei were counterstained with 1:10,000 DAPI and coverslips mounted with Prolong® Gold Antifade

457 Reagent. Duodenum, jejunum, and ileum were defined as the proximal, middle, and distal third of the
458 small intestine. Proximal colon was defined as the proximal 4cm of the large intestine, and distal colon as
459 the distal 4cm. For alkaline phosphatase staining, we used the Vector® Red Substrate Kit, Alkaline
460 Phosphatase (Vector Laboratories SK-5100) on deparaffinized slides as described in the manufacturer's
461 protocol. TUNEL was detected using the Click-iT™ Plus TUNEL Assay for In Situ Apoptosis Detection,
462 Alexa Fluor™ 594 dye (Thermo Scientific C10618). All stains were imaged on the Keyence BZ-X100.
463

464 **Histopathology and appearance scoring**

465 Histopathological scoring was performed by blinded anatomical pathologist Dr. Benjamin Wilkins based
466 on previously published criteria with an additional score for villus damage for small intestine
467 (Supplemental Table 2) (55). For each category, the recorded score reflects the most severe finding. For
468 percent involvement, the recorded score reflects the length of bowel that was involved by any of the
469 scored processes. Scores were summed for each mouse to generate a separate composite score for
470 small intestine and colon. Mouse appearance/behavior was scored according to a previously described
471 rubric (56).
472

473 **Intestinal epithelial organoid cultures**

474 Intestinal sections were splayed open, rinsed in PBS, and rotated at 4°C for 45 minutes in Hank's
475 Buffered Saline Solution with 10 mM EDTA and 1 mM N-Acetyl-L-cysteine (Sigma A9165). Crypts were
476 isolated by scraping with a glass coverslip followed by vortexing and filtering through a 70 uM (small
477 intestine) or 100 uM (colon) cell strainer. Crypt-enriched suspensions were centrifuged at 500xG, 25˚C
478 for 5 minutes, washed in PBS, and pelleted again at 500xG, 25˚C for 5 minutes. Crypts were plated in
479 Matrigel droplets (Corning 354234) and unless stated otherwise, overlaid with the following "ENR"
480 medium: advanced DMEM/F12 media (Thermo 12634028) containing 1X GlutaMAX (Thermo 35050061),
481 10 mM HEPES (Thermo 15-630-080), 1X Antibiotic Antimycotic (Thermo 15240062), 1X N-2 Supplement
482 (Thermo 17502048), 1X B-27 Supplement (Thermo 17504044), 5 μM CHIR99021 (Cayman 13122), 1 mM
483 N-Acetyl-L-cysteine (Sigma A9165), 50 ng/mL mEGF (PeproTech 315-09), 5% Noggin/R-spondin
484 conditioned medium (generated using protocol from (32)), and 10 μM Y-27632 (LC Labs Y-5301). Colonic

485 epithelial cultures were fed 50% WRN CM media (57). Passage-matched enteroids/colonoids were used
486 for all experiments. For induction of CreERT2, enteroids/colonoids were given 1 μM 4-OHT in 100%
487 ethanol at 48 and 24 hours before the start of the time course then mechanically passaged at day 0.
488

489 **Whole mount staining in enteroids**

490 Enteroids were dissociated to single cells using Accutase (STEMCELL Technologies 07920),
491 resuspended in ENR supplemented with 10 μM Y-27632, and plated on chamber slides pretreated with
492 10% Matrigel in Advanced DMEM/F12. The next day, slides were incubated in 4% PFA at room
493 temperature for 20 minutes and blocked in 10% goat serum in PBS for 30 minutes at 25°C. 1:200 rabbit
494 monoclonal anti-METTL3 (abcam ab195352) and 1:200 goat polyclonal anti-E-Cadherin (R&D Systems
495 AF748) were used at 37°C for 30 minutes, followed by 1:600 Alexa Fluor 488 AffiniPure Bovine Anti-goat
496 IgG (Jackson 805-545-180) and Cy3 AffiniPure Donkey Anti-Rabbit IgG (Jackson 711-165-152) in PBS
497 supplemented with 1:5000 DAPI. Chambers were detached from the chamber slide and coverslips
498 mounted with Prolong® Gold Antifade Reagent.
499

500 **qRT-PCR**

501 RNA was isolated using the Quick-RNA Miniprep Kit (Zymo R1054). RNA was reverse transcribed using
502 MultiScribe™ Reverse Transcriptase (Thermo Scientific 4311235) with random hexamer primers.
503 Quantitative PCR was performed using the Applied Biosystems TaqMan Fast Advanced Master Mix
504 (Thermo Scientific 4444556) with TaqMan™ Gene Expression Assay (FAM) primers (Supplemental Table
505 3**)** on an Applied Biosystems QuantStudio 3.
506

507 **Western blotting**

508 Cells were lysed using RIPA buffer (CST 9806S) supplemented with 1:100 protease phosphatase
509 inhibitor (CST 5872S) and protein concentration was measured using the Pierce™ BCA Protein Assay Kit
510 (Thermo 23225). Lysates were boiled for 5 minutes with 100 mM DTT and 1X LDS buffer (GenScript
511 M00676) and run on NuPAGE 4-12% Bis-Tris gels (Thermo NP0335BOX) in 1X MOPS-SDS buffer
512 (BioWorld 10530007-2) or 1X MES-SDS buffer (Thermo NP0002, use for low MW proteins). Gels were

513 transferred onto PVDF transfer membrane in 2X NuPAGE transfer buffer (Thermo NP006) and
514 membranes blocked for 1 hr in 5% milk in TBS-T (TBS, 0.1% Tween-20), and then placed in 1:1000
515 primary antibody (Supplementary Table 1) overnight in 5% milk in TBS-T at 4˚C. Blots were washed in
516 TBS-T and placed in 1:2000 secondary antibody (Supplementary Table 1) for 1-2 hours at 25˚C. Blots
517 were then subjected to Supersignal® West Femto Maximum Sensitivity Chemiluminescent Substrate and
518 imaged on the Biorad Gel Doc XR.
519
520 **m^6A dot blot**
521 mRNA was isolated using the Dynabeads™ mRNA DIRECT™ Purification Kit (Thermo 61011). >30 ng of
522 mRNA was heated to 65°C for 2 minutes, placed on ice for >5 minutes, and then pipetted onto a Hybond
523 N+ nitrocellulose membrane and exposed to 254 nm UV light for 5 minutes. The nitrocellulose membrane
524 was then washed in TBS-T (TBS, 0.1% Tween-20). Blots were then incubated in primary and secondary
525 antibody and developed as described in the section on Western blotting. We detected m^6A using anti-m^6A
526 primary antibody CST 56593. Total blotted mRNA was stained using 0.04% Methylene Blue (LabChem
527 LC168508) in 0.5M sodium acetate.
528
529 **RNA-seq and Ribo-seq**
530 Ileal enteroids were expanded in Matrigel in 50% WRN media until 8 to 10 million cells per replicate was
531 achieved. Passage separated replicates from the same enteroid line were used. Media was
532 supplemented with 2 uM 4-OHT 72 hours prior to collection. Enteroids were collected by mechanical
533 dissociation, pelleted, and snap frozen in liquid nitrogen. Frozen enteroid pellets were resuspended in ice-
534 cold lysis buffer containing 20mM Tris-HCl pH 7.4, 150mM MgCl2, 150mM NaCl, 100ug/ml
535 cycloheximide, 1% v/v Triton X-100, 1mM DTT, 1U/ul SUPERase·IN RNase inhibitor (ThermoFisher),
536 25U/ml Turbo DNase1 (ThermoFisher), and 1X EDTA-free protease inhibitor cocktail (Roche). Cells were
537 lysed by trituration through a 26-gauge needle 10 times. Samples were processed and libraries prepared
538 as previously described (39) with the following modifications. First, we performed sucrose cushion to
539 pellet the ribosome-associated mRNAs and proceeded with RNAse I digestion (10 U/µl by the Epicentre
540 definition) for 30ug of RNA. Samples were incubated at room temperature for 45 minutes with gentle

541 agitation, and the digestion was quenched by adding 200 units of SUPERase·IN. Then, we directly
542 extracted the ribosome-protected fragments (RPF) using the TRIzol reagent and performed gel size
543 selection of the RPFs of 15-35 nucleotides in length. Second, we performed rRNA depletion using
544 RiboCop for Human/Mouse/Rat kit (Lexogen). Once the rRNA-depleted RPF fragments were obtained,
545 they were pooled together, and the libraries prepared with Unique molecular identifiers (UMIs) for
546 deduplication. The multiplexed library was then sequenced on Illumina HiSeq 4000 with PE150 runs
547 (paired end reading of 150 bases), with a sequencing depth of 60 million raw reads/sample. For each
548 sample, one-tenth (150ul) of the lysate was saved for RNA-seq. For RNA-seq, total RNA was extracted
549 using TRIzol LS reagent (Ambion) and purified using Quick-RNA Microprep kit (Zymo) following the
550 manufacturer's protocol. Libraries were prepared from total RNA using the Smarter® Stranded Total
551 RNA-Seq Kit v2 - Pico Input Mammalian (Takara Bio 634411) and sequenced on a Novaseq 6000, SP
552 Reagent Kit 1.5 (100 cycles). Raw sequencing data were demultiplexed, adaptors were removed using
553 cutadapt (58), contaminant sequences (rRNA and tRNA) were depleted, and reads were deduplicated
554 (umi_tools dedup). Reads were aligned to all transcripts on the mouse reference chromosomes (Gencode
555 version M31, GRCm39) using Kallisto (59). Translation efficiency (TE) was calculated by dividing the TPM
556 in the total RNA library by the TPM in the RPF library for each individual transcript and sample. Pathway
557 enrichment analysis was performed using mouse gene symbols orthology-mapped to the human genome
558 and tested against Gene Ontology Biological Process (GOBP) gene sets with the Molecular Signatures
559 Database (gsea-msigdb.org).
560

561 **m^6A-seq**

562 Three wildtype C57BL/6J mice (Jax #000664, 2 male 1 female) aged 8 weeks were used. Crypts were
563 isolated from the distal half of the small intestine as described above and dissociated in 10% FBS in 1X
564 PBS supplemented with 20 µg/mL Liberase TH (Roche 05401135001), and 35 µg/ml DNaseI (Roche
565 10104159001) for 20 minutes at 37°C with frequent agitation. Cell suspensions were then stained with
566 1:200 PE-EpCAM (BioLegend 118205), 1:200 FITC-CD45 (BioLegend 103107), and 1:1000 DRAQ7
567 (Thermo Scientific D15106) on ice for 30 minutes in the dark. ~800K live epithelial cells per mouse were
568 then isolated by flow cytometry by sorting for DRAQ7- CD45- PE+ cells directly into Trizol LS (Ambion 10-

569 296-010) on a FACSJazz Sorter. RNA was isolated from Trizol LS using the Direct-zol RNA Microprep Kit
570 (Zymo R2062). RIP-seq was performed according to the "Refined RIP-seq" protocol for low input material
571 (40) with the following specifications: 2 µg anti-m^{6}A antibody (Synaptic Systems 202 003) was conjugated
572 to magnetic beads and incubated with 6 ug total RNA that was previously fragmented to ~300 nt
573 fragments with 10 mM ZnCl2 in 10 mM Tris-HCl for 4 minutes at 70°C (5% of fragmented RNA was set
574 aside as input). After 2 hours immunoprecipitation at 4°C, RNA-bead complexes were washed in high and
575 low salt buffer and RNA was eluted from the RNA-bead complexes using the Qiagen RNeasy Plus Micro
576 Kit (Qiagen 74034). Isolated m^{6}A-enriched RNA was immunoprecipitated a second time using 2 µg of a
577 second anti-m^{6}A antibody (Abcam ab151230). Final cDNA Libraries were prepared from twice
578 immunoprecipitated RNA and fragmented input total RNA using the Smarter® Stranded Total RNA-Seq
579 Kit v2 - Pico Input Mammalian (Takara Bio 634411) and sequenced on a Novaseq 6000, SP Reagent Kit
580 1.5 (100 cycles). Raw reads were aligned to mm10 (gencode_M23_GRCm38.p6) using STAR aligner
581 (2.7.9a). N6-methyladenosine peaks were identified using exomePeak2 (version 1.2.0), followed by a
582 metagene analysis using the bioconducter packages Guitar_2.10.0 and
583 TxDb.Mmusculus.UCSC.mm10.knownGene_3.10.0.
584

585 **m^{6}A-RIP-qPCR**

586 For m^{6}A-RIP-qPCR, four *Mettl3*$^{flox/flox}$ and four *Mettl3*$^{VilCreER\Delta/\Delta}$ mice aged 8 weeks were used (2 male, 2
587 female mice per genotype). Intestinal crypts were isolated from the distal half of the small intestine as
588 described above but without digestion to single cells. Whole crypts were pelleted, resuspended in TRI
589 Reagent (Sigma 93289), and RNA was isolated using the Direct-zol RNA Miniprep Kit (Zymo R2050).
590 Next, 20 µg of total RNA was fragmented and immunoprecipitated twice according to the "Refined RIP-
591 seq protocol" as described above. Immunoprecipitated RNA and fragmented input total RNA was reverse
592 transcribed using the High-Capacity cDNA Reverse Transcription Kit (Thermo 4368814) and qPCR was
593 performed as described in the "qRT-PCR" section. For calculation of m^{6}A enrichment, first we calculated
594 the %input for every target in every RIP sample as 2^-(Ct of target gene in RIP – Ct of target gene in input
595 sample). Then we calculated m^{6}A enrichment relative to *Gapdh* by dividing the %input of the target of
596 interest (e.g., *Kras 5' or 3'UTR)* by the %input of *Gapdh* for each sample.

597

598 **Lentiviral constructs and transduction**

599 Accutase-digested (STEMCELL Technologies 07920) enteroids were resuspended in ENR with 1:4
600 lentivirus solution, TransDux MAX Lentivirus Transduction Enhancer (System Biosciences LV860A-1),
601 and 10 uM Y-27632 and plated as monolayers on Collagen I (Advanced Biomatrix 5010). Lentiviral
602 constructs and prepared virus were generated by VectorBuilder. The transfer vector for catalytic inactive
603 METTL3 expression contained a CMV-EGFP:T2A:Puro selection cassette and the mPGK promoter
604 upstream of the *Mus musculus Mettl3* ORF edited at positions 1183-1194 from GACCCACCTTGG to
605 GCCCCACCTGCG yielding DPPW -> APPA synonymous mutation in the catalytic site as previously
606 described (33). The "GFP" control vector contained a CMV-mCherry:T2A:Puro selection cassette and the
607 EGFP ORF under control of the CMV promoter. After overnight incubation with lentivirus, enteroid
608 monolayers were mechanically dissociated and replated as 3D enteroids in Matrigel and selected for
609 antibiotic resistance genes after 48 hours.

610

611 **Quantification and statistical analysis**

612 Unless otherwise noted, quantification of immunofluorescent staining was performed using three
613 representative images taken per mouse using a 20X objective. Images were taken in three areas of most
614 severe histological distortion (defined as a high-powered field with greatest changes in crypt and/or villus
615 morphology) in distal half of the small intestine of tested mice. Three representative sections were chosen
616 from matching regions of the distal half of the small intestine in control mice. Quantification was
617 performed by individuals blinded to mouse genotype. Unless otherwise noted, each graphed data point is
618 the mean of three quantified representative images per mouse. P values were calculated with the
619 unpaired parametric Student's t test in GraphPad Prism. P values for survival curves were calculated
620 using the Log-rank Mantel-Cox test in GraphPad Prism.

621

622 **Study approval**

623 Mouse experiments and handling were approved under IACUC protocol 001278 at the Children's Hospital
624 of Philadelphia.

Data and materials availability:

All data needed to evaluate the conclusions in the paper are present in the paper and/or the Supplementary Materials. Raw sequencing data are uploaded to Dryad at https://doi.org/10.5061/dryad.5tb2rbp8s.

Author contributions:

Conceptualization: CHD, KEH

Methodology: CHD, EAM, SV, PS

Formal analysis: CHD, KEH[2], SV, YZ, BJW

Investigation: CHD, KEN, SV, RM, SKN, KK, LP, XM, AC

Visualization: CHD, KEH[2]

Supervision: CHD, KEH, PS, MDW

Writing—original draft: CHD, KEH

Writing—review & editing: CHD, KEH, MDW, KEN, KK

KEH: Katharyn E. Hamilton

KEH[2]: Katharina E. Hayer

Acknowledgments

We thank Dr. Richard Flavell (Yale University), Dr. Federica Accornero (Ohio State University), and Dr. Brian Capell (University of Pennsylvania Perelman School of Medicine) for generously providing Mettl3-floxed mice used in this study. For feedback, technical assistance, and/or sharing of laboratory reagents, we thank: Dr. Michael Silverman, Dr. Michael Abt, Dr. Tatiana Karakasheva, Gloria Soto, Dr. Amanda Muir, Dr. Masaru Sasaki, Joshua Wang, Dr. Lan Lin, Dr. Samir Adhikari, Dr. Derek Sung, and Nora Kiledjian (Children's Hospital of Philadelphia/University of Pennsylvania Perelman School of Medicine) and Dr. Igor Brodsky, Dr. Chris Lengner, and Zvi Cramer (University of Pennsylvania School of Veterinary Medicine). We also thank the following scientific cores and centers: The Center for Molecular Studies in

Digestive and Liver Diseases (P30DK050306) and the Molecular Pathology and Imaging Core (RRID: SCR_022420), the Flow Cytometry Core at the Children's Hospital of Philadelphia, and the Center for Applied Genomics at the Children's Hospital of Philadelphia. Artwork depicting mouse injection schemes was created with BioRender.com

Funding:

NIDDK R01-DK124369 (KEH)

NIEHS R21-ES031533 (KEH)

The Children's Hospital of Philadelphia Institutional Development Funds (KEH)

The Gastrointestinal Epithelium Modeling Program (KEH)

References

1. Peterson LW, Artis D. Intestinal epithelial cells: Regulators of barrier function and immune homeostasis. *Nat. Rev. Immunol.* 2014;14(3):141–153.
2. Gehart H, Clevers H. Tales from the crypt: new insights into intestinal stem cells [Internet]. *Nat. Rev. Gastroenterol. Hepatol.* 2019;16(1):19–34.
3. Yousefi M, Li L, Lengner CJ. Hierarchy and Plasticity in the Intestinal Stem Cell Compartment. *Trends Cell Biol.* 2017;27(10):753–764.
4. Sanman LE et al. Transit-Amplifying Cells Coordinate Changes in Intestinal Epithelial Cell-Type Composition [Internet]. *Dev. Cell* 2021;56(3):356-365.e9.
5. Ding X et al. Crypt Base Columnar Stem Cells in Small Intestines of Mice Are Radioresistant. *Gastroenterology* 2012;16(3):387–393.
6. Gibson RJ, Bowen JM, Inglis MRB, Cummins AG, Keefe DMK. Irinotecan causes severe small intestinal damage, as well as colonic damage, in the rat with implanted breast cancer. *J. Gastroenterol. Hepatol.* 2003;18(9):1095–1100.
7. Sansom OJ et al. MBD4 deficiency reduces the apoptotic response to DNA-damaging agents in the murine small intestine. *Oncogene* 2003;22(46):7130–7136.
8. Chen G, Han Y, Zhang H, Tu W, Zhang S. Radiotherapy-Induced Digestive Injury: Diagnosis, Treatment and Mechanisms. [Internet]. *Front. Oncol.* 2021;11:757973.
9. Di Fiore F, Van Cutsem E. Acute and long-term gastrointestinal consequences of chemotherapy. [Internet]. *Best Pract. Res. Clin. Gastroenterol.* 2009;23(1):113–24.
10. Secombe KR, Coller JK, Gibson RJ, Wardill HR, Bowen JM. The bidirectional interaction of the gut microbiome and the innate immune system: Implications for chemotherapy-induced gastrointestinal toxicity [Internet]. *Int. J. Cancer* 2019;144(10):2365–2376.
11. Chatterji P et al. Posttranscriptional regulation of colonic epithelial repair by RNA binding protein IMP1/ IGF2BP1. *EMBO Rep.* 2019;20(6):1–16.
12. Chatterji P et al. The LIN28B–IMP1 post-transcriptional regulon has opposing effects on oncogenic signaling in the intestine. *Genes Dev.* 2018;32(15–16):1020–1034.
13. Han B et al. YTHDF1-mediated translation amplifies Wnt-driven intestinal stemness. *EMBO Rep.* 2020;1–14.
14. Jabs S et al. Impact of the gut microbiota on the m6A epitranscriptome of mouse cecum and liver [Internet]. *Nat. Commun.* 2020;11(1):1–16.
15. Olazagoitia-Garmendia A et al. Gluten-induced RNA methylation changes regulate intestinal

698 inflammation via allele-specific XPO1 translation in epithelial cells. *Gut* 2022;71(1):68–77.
699 16. Meyer KD et al. Comprehensive analysis of mRNA methylation reveals enrichment in 3′ UTRs and
700 near stop codons. *Cell* 2012;149(7):1635–1646.
701 17. Dominissini D et al. Topology of the human and mouse m6A RNA methylomes revealed by m6A-seq.
702 *Nature* 2012;485(7397):201–206.
703 18. Murakami S, Jaffrey SR. Hidden codes in mRNA: Control of gene expression by m6A [Internet]. *Mol.*
704 *Cell* 2022;82(12):2236–2251.
705 19. Jabs S et al. Impact of the gut microbiota on the m6A epitranscriptome of mouse cecum and liver.
706 *Nat. Commun.* 2020;11(1). doi:10.1038/s41467-020-15126-x
707 20. Zhang J et al. m6A modification in inflammatory bowel disease provides new insights into clinical
708 applications [Internet]. *Biomed. Pharmacother.* 2023;159:114298.
709 21. Wang P, Doxtader KA, Nam Y. Structural Basis for Cooperative Function of Mettl3 and Mettl14
710 Methyltransferases.. *Mol. Cell* 2016;63(2):306–317.
711 22. Wang X et al. Structural basis of N6-adenosine methylation by the METTL3-METTL14 complex.
712 *Nature* 2016;534(7608):575–578.
713 23. Zhang T et al. m6A mRNA modification maintains colonic epithelial cell homeostasis via NF-κB-
714 mediated antiapoptotic pathway. *Sci. Adv.* 2022;8(12). doi:10.1126/sciadv.abl5723
715 24. Du J et al. N6-adenomethylation of GsdmC is essential for Lgr5+ stem cell survival to maintain normal
716 colonic epithelial morphogenesis [Internet]. *Dev. Cell* [published online ahead of print: August 2022];
717 doi:10.1016/j.devcel.2022.07.006
718 25. Liu Y et al. Segregation of the stemness program from the proliferation program in intestinal stem
719 cells [Internet]. *Stem Cell Reports* 2023;18. doi:10.1016/j.stemcr.2023.03.007
720 26. Madison BB et al. Cis Elements of the Villin Gene Control Expression in Restricted Domains of the
721 Vertical (Crypt) and Horizontal (Duodenum, Cecum) Axes of the Intestine [Internet]. *J. Biol. Chem.*
722 2002;277(36):33275–33283.
723 27. Wang A et al. m6A modifications regulate intestinal immunity and rotavirus infection [Internet]. *Elife*
724 2022;11. doi:10.7554/eLife.73628
725 28. Gustafsson JK, Johansson MEV. The role of goblet cells and mucus in intestinal homeostasis. *Nat.*
726 *Rev. Gastroenterol. Hepatol.* 2022;19(12):785–803.
727 29. Wallaeys C, Garcia-Gonzalez N, Libert C. Paneth cells as the cornerstones of intestinal and
728 organismal health: a primer. *EMBO Mol. Med.* 2022;1–26.
729 30. Li H-B et al. m6A mRNA methylation controls T cell homeostasis by targeting the IL-7/STAT5/SOCS
730 pathways [Internet]. *Nature* 2017;548(7667):338–342.
731 31. Shay Geula, Sharon Moshitch-Moshkovitz, Dan Dominissini, Abed AlFatah Mansour, Nitzan Kol, Mali
732 Salmon-Divon, Vera Hershkovitz, Eyal Peer, Nofar Mor, Yair S. Manor, Moshe Shay Ben-Haim, Eran
733 Eyal, Sharon Yunger, Yishay Pinto, Diego Adhemar Jaitin JHH. m6A mRNA methylation facilitates
734 resolution of naïve pluripotency toward differentiation. *Science (80-.).* 2015;347(6225):1002–1006.
735 32. Sato T et al. Single Lgr5 stem cells build crypt-villus structures in vitro without a mesenchymal niche.
736 *Nature* 2009;459(7244):262–265.
737 33. Clancy MJ, Shambaugh ME, Timpte CS, Bokar JA. Induction of sporulation in Saccharomyces
738 cerevisiae leads to the formation of N6-methyladenosine in mRNA: A potential mechanism for the activity
739 of the IME4 gene. *Nucleic Acids Res.* 2002;30(20):4509–4518.
740 34. Lin S, Choe J, Du P, Triboulet R, Gregory RI. The m6A Methyltransferase METTL3 Promotes
741 Translation in Human Cancer Cells [Internet]. *Mol. Cell* 2016;62(3):335–345.
742 35. Choe J et al. mRNA circularization by METTL3–eIF3h enhances translation and promotes
743 oncogenesis [Internet]. *Nature* 2018;561(7724):556–560.
744 36. Wei X et al. METTL3 preferentially enhances non-m6A translation of epigenetic factors and promotes
745 tumourigenesis. *Nat. Cell Biol.* 2022;24(8):1278–1290.
746 37. Zaccara S, Jaffrey SR. A Unified Model for the Function of YTHDF Proteins in Regulating m6A-
747 Modified mRNA [Internet]. *Cell* 2020;181(7):1582-1595.e18.
748 38. Meyer KD et al. 5′ UTR m6A Promotes Cap-Independent Translation [Internet]. *Cell* 2015;163(4):999–
749 1010.
750 39. Cope AL et al. Exploring Ribosome-Positioning on Translating Transcripts with Ribosome Profiling.
751 [Internet]. *Methods Mol. Biol.* 2022;2404:83–110.
752 40. Zeng Y et al. Refined RIP-seq protocol for epitranscriptome analysis with low input materials. *PLoS*
753 *Biol.* 2018;16(9):1–20.

754 41. Ternet C, Kiel C. Signaling pathways in intestinal homeostasis and colorectal cancer: KRAS at centre
755 stage [Internet]. *Cell Commun. Signal.* 2021;19(1):1–22.
756 42. Liu J et al. Landscape and Regulation of m6A and m6Am Methylome across Human and Mouse
757 Tissues. *Mol. Cell* 2020;77(2):426-440.e6.
758 43. Garmendia I, Redin E, Montuenga LM, Calvo A. YES1: A Novel Therapeutic Target and Biomarker in
759 Cancer. *Mol. Cancer Ther.* 2022;21(9):1371–1380.
760 44. Niu X et al. The nuclear pore complex function of sec13 protein is required for cell survival during
761 retinal development. *J. Biol. Chem.* 2014;289(17):11971–11985.
762 45. Groen EJN, Gillingwater TH. UBA1: At the Crossroads of Ubiquitin Homeostasis and
763 Neurodegeneration [Internet]. *Trends Mol. Med.* 2015;21(10):622–632.
764 46. Alexander PB et al. EGF promotes mammalian cell growth by suppressing cellular senescence.
765 [Internet]. *Cell Res.* 2015;25(1):135–8.
766 47. Fang T et al. Epidermal growth factor receptor-dependent DNA repair promotes murine and human
767 hematopoietic regeneration. [Internet]. *Blood* 2020;136(4):441–454.
768 48. Bohin N, Carlson EA, Samuelson LC. Genome Toxicity and Impaired Stem Cell Function after
769 Conditional Activation of CreER T2 in the Intestine [Internet]. *Stem Cell Reports* 2018;11(6):1337–1346.
770 49. Tóth B, Ben-Moshe S, Gavish A, Barkai N, Itzkovitz S. Early commitment and robust differentiation in
771 colonic crypts. *Mol. Syst. Biol.* 2017;13(1):902.
772 50. Qu M et al. Establishment of intestinal organoid cultures modeling injury-associated epithelial
773 regeneration [Internet]. *Cell Res.* [published online ahead of print: January 8, 2021]; doi:10.1038/s41422-
774 020-00453-x
775 51. Liu Y et al. Dissecting the Role of the FGF19-FGFR4 Signaling Pathway in Cancer Development and
776 Progression. *Front. Cell Dev. Biol.* 2020;8(February):1–9.
777 52. Boissier P, Huynh-Do U. The guanine nucleotide exchange factor Tiam1: A Janus-faced molecule in
778 cellular signaling [Internet]. *Cell. Signal.* 2014;26(3):483–491.
779 53. Peeters M et al. Prevalence of RAS mutations and individual variation patterns among patients with
780 metastatic colorectal cancer: A pooled analysis of randomised controlled trials. [Internet]. *Eur. J. Cancer*
781 2015;51(13):1704–13.
782 54. Johnson L et al. K-ras is an essential gene in the mouse with partial functional overlap with N-ras.
783 *Genes Dev.* 1997;11(19):2468–2481.
784 55. Dieleman LA et al. Chronic experimental colitis induced by dextran sulphate sodium (DSS) is
785 characterized by Th1 and Th2 cytokines. [Internet]. *Clin. Exp. Immunol.* 1998;114(3):385–91.
786 56. Paster E V, Villines KA, Hickman DL. Endpoints for mouse abdominal tumor models: refinement of
787 current criteria. [Internet]. *Comp. Med.* 2009;59(3):234–41.
788 57. Miyoshi H, Stappenbeck TS. In vitro expansion and genetic modification of gastrointestinal stem cells
789 in spheroid culture. *Nat. Protoc.* 2013;8(12):2471–2482.
790 58. Martin M. Cutadapt removes adapter sequences from high-throughput sequencing reads [Internet].
791 *EMBnet.journal* 2011;17(1):10.
792 59. Bray NL, Pimentel H, Melsted P, Pachter L. Near-optimal probabilistic RNA-seq quantification
793 [Internet]. *Nat. Biotechnol.* 2016;34(5):525–527.
794
795

Figures

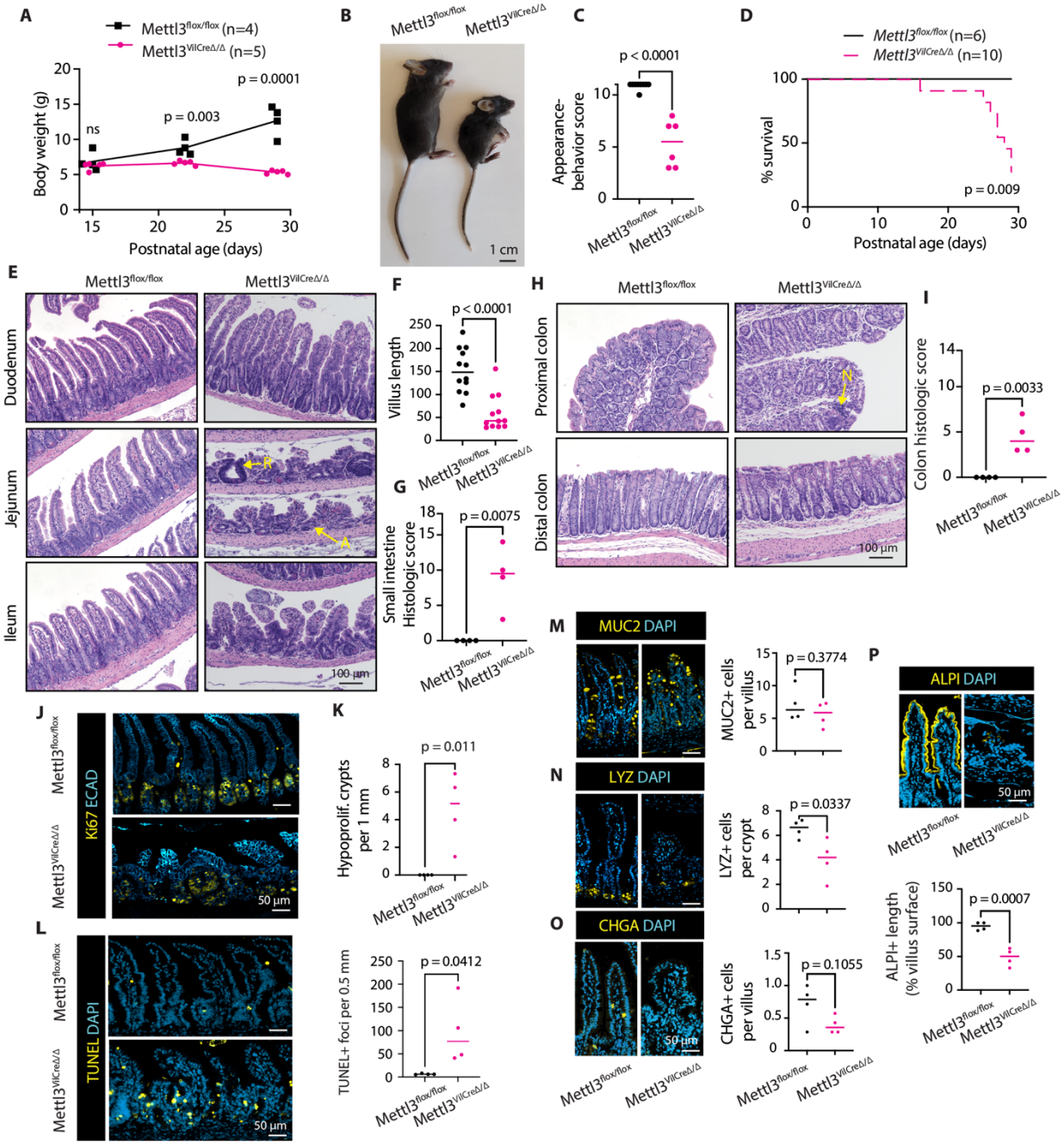

Figure 1. Constitutive METTL3 deletion leads to growth retardation and small intestinal epithelial distortion. (A) Growth curves from postnatal day 15 to 29**. (B)** Gross appearance at postnatal day 29. **(C)** Composite appearance and behavior score at postnatal day 29. **(D)** Kaplan-Meier survival curves through postnatal day 29; p value corresponds to Log-rank (Mantel-Cox) test. **(E)** Representative small intestine H&E images. "R" indicates regenerative crypt. "A" indicates atrophic crypt. **(F)** Quantification of jejunal villus lengths, n=4 mice per genotype. **(G)** Composite histological score for small intestine **(H)** Representative colon H&E images. "N" denotes neutrophil invasion. **(I)** Composite histological score for colon **(J)** Representative images of Ki67 in distal small intestine **(K)** Number of hypo-proliferative crypts (<10 Ki67+ cells) crypts per 1 mm distal half small intestine **(L)** Representative images and quantification of TUNEL

808 staining **(M, N, O)** Representative images and quantification of intestinal secretory markers MUC2, LYZ,
809 and CHGA **(P)** Representative images and quantification of alkaline phosphatase. Unless otherwise noted,
810 each data point is the mean of three representative sections imaged per mouse with bar at median value
811 and p value represents unpaired parametric Student's t test. Immunofluorescence staining and
812 quantification performed in distal half small intestine.

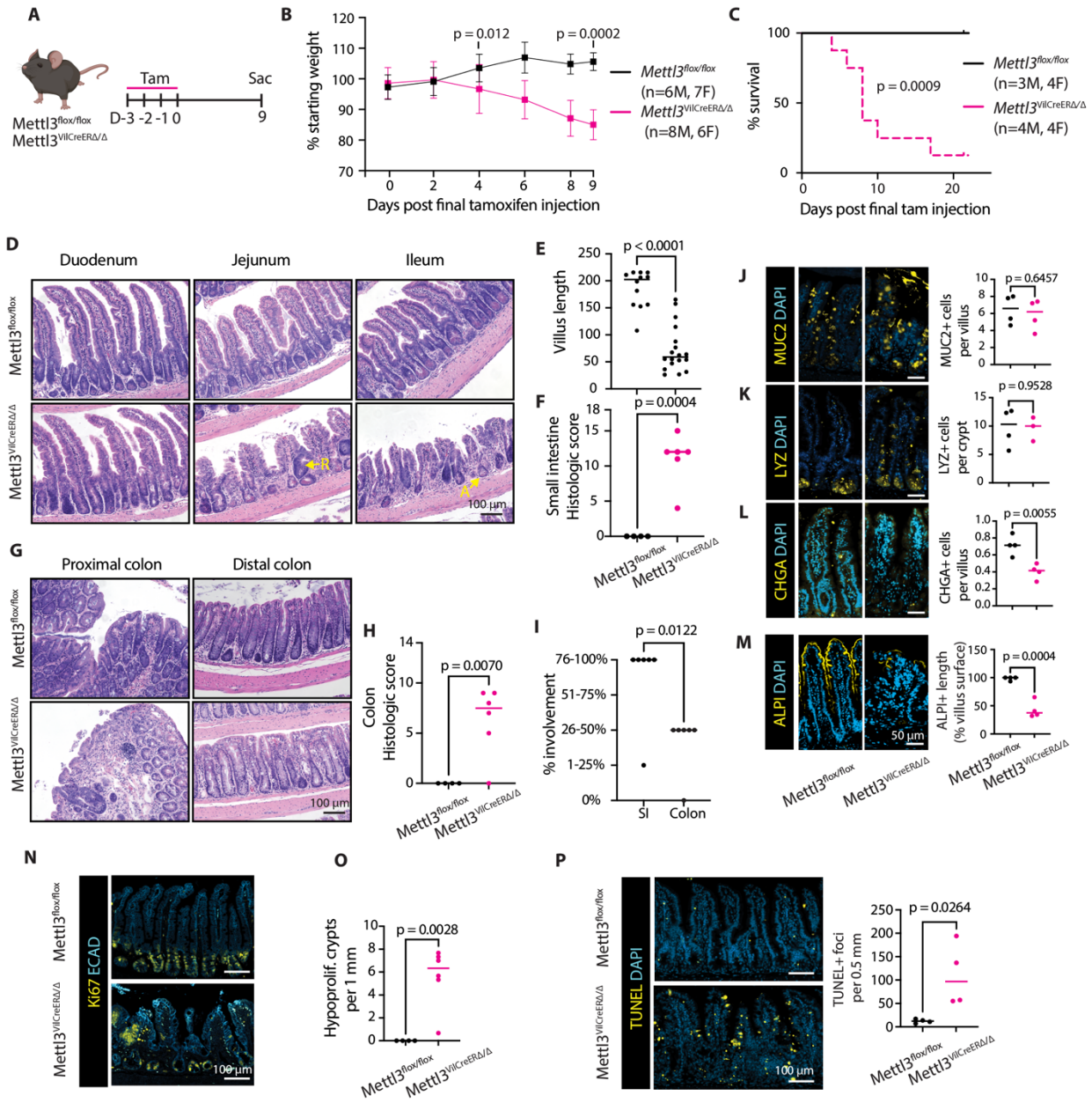

Figure 2. METTL3 is required for survival and small intestinal epithelial homeostasis in adult mice. **(A)** Experimental schematic depicting timing of tamoxifen injection. **(B)** Weight curves through nine days post tamoxifen injection, mean +/- SD. **(C)** Kaplain-Meier survival curves through 22 days post final tamoxifen injecition, p value corresponds to Log-rank (Mantel-Cox) test. **(D)** Representative small intestine H&E images. "R" indicates regenerative crypt. "A" indicates atrophic crypt. **(E)** Quantification of shortest villus lengths in three representative jejunal sections in *Mettl3*$^{flox/flox}$ (n=4) and *Mettl3*$^{VilCreER\Delta/\Delta}$ (n=6) mice. **(F)** Composite histological score for small intestine. **(G)** Representative colon H&E images. **(H)** Composite histological score for colon. **(I)** Greatest percent involvement for histological score depicted in F or H. **(J, K, L)** Representative images and quantification of intestinal secretory markers MUC2, LYZ, and CHGA. **(M).** Representative images and quantification of alkaline phosphatase activity. **(N)** Representative images of Ki67 **(O)** Number of hypo-proliferative (<10 Ki67+ cells) crypts per 1mm intestine **(P)** Representative images

826 and quantification of TUNEL staining. Unless otherwise noted, each data point is the mean of three
827 representative sections per mouse with bar at median value and p value represents unpaired parametric
828 Student's t test. Immunofluorescence staining and quantification performed in distal half small intestine.
829

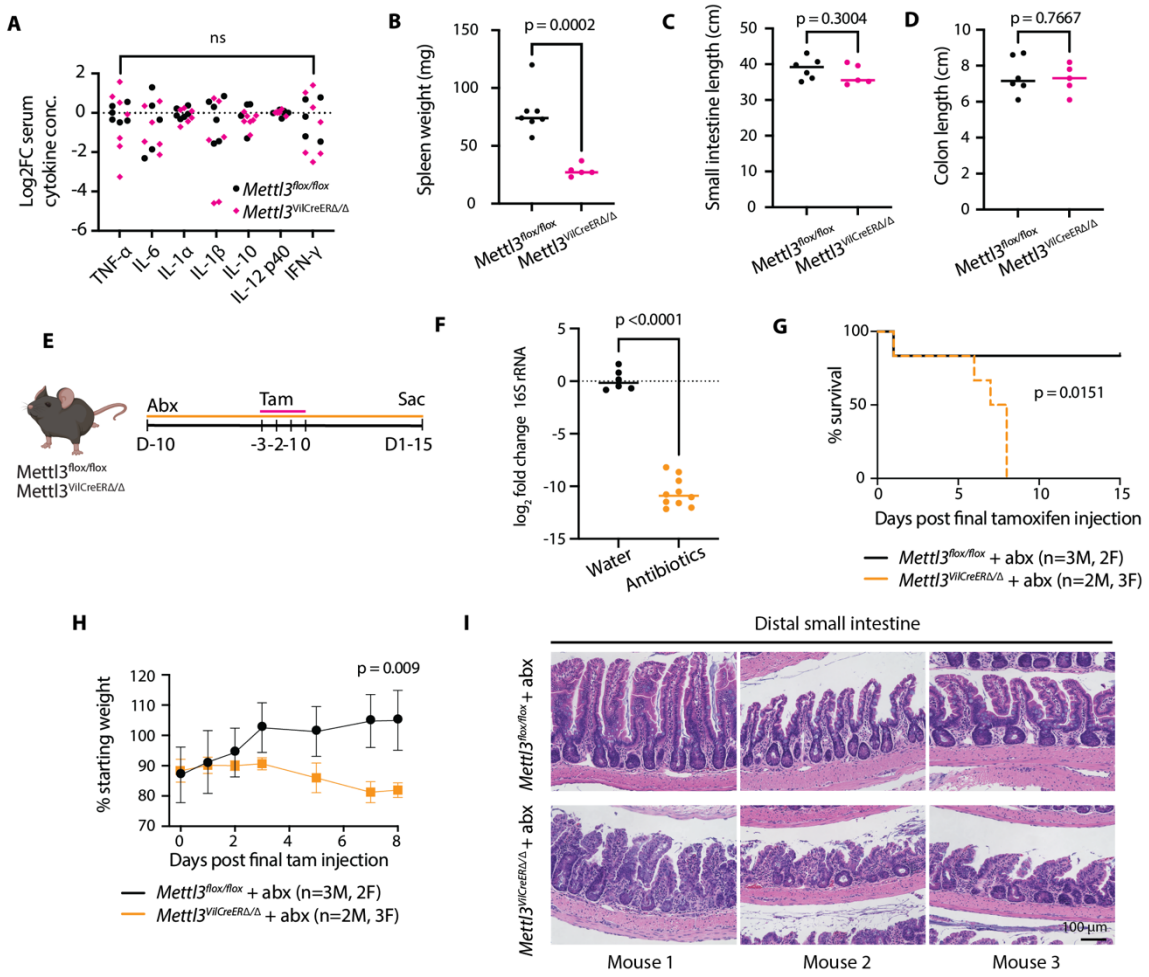

Figure 3. Intestinal distortion and mortality after METTL3 deletion is microbiota independent. (A) Log_2 fold change in serum cytokines in mice nine days post final tamoxifen injection, ns indicates $p > 0.05$ for all. **(B)** Spleen weight nine days post final tamoxifen injection. **(C, D)** Small intestine and colon length nine days post final tamoxifen injection. **(E)** Experimental schematic for antibiotic (abx) treatment. **(F)** Log_2 fold change in 16S rRNA amplified from fecal bacterial DNA on final day of tamoxifen injection in antibiotic-treated or water vehicle mice. **(G, H)** Kaplain-Meier survival curve and weight change post final tamoxifen injection in antibiotic treated mice. P-value in (G) represents Log-rank (Mantel-Cox) test. Data in (H) presented as mean +/- SD **(I)** Representative H&E images from matched sections of distal small intestine in n=3 antibiotic treated mice per genotype. Unless otherwise noted, each data point represents a single mouse with bar at median value and p denotes value of unpaired parametric Student's t test.

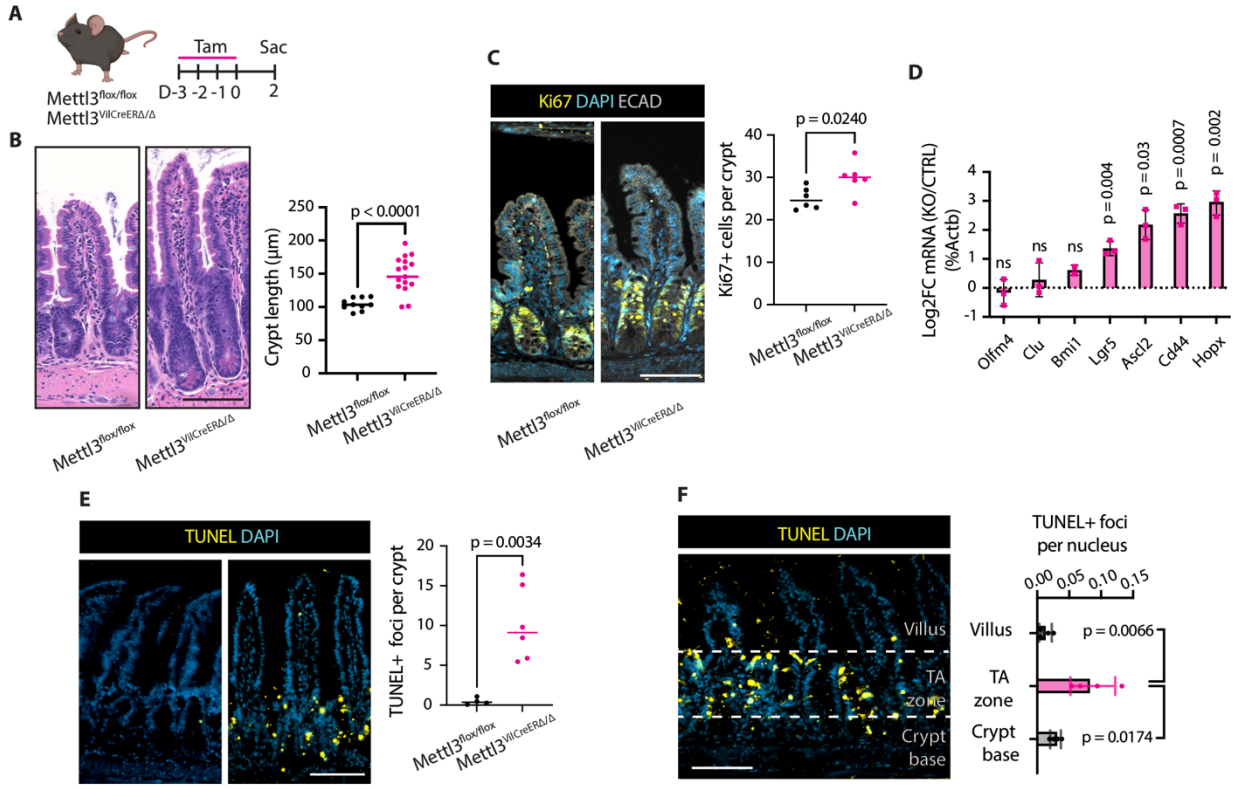

Figure 4. METTL3 deletion rapidly induces death of transit amplifying cells. (A) Experimental schematic. **(B)** Representative images and quantification of crypt height. **(C)** Representative images and quantification of Ki67 staining. **(D)** Log_2 fold change in qPCR quantification of indicated genes normalized to the mean of *Mettl3*$^{flox/flox}$ controls and *Actb*. Data from crypt enriched lysates. **(E)** Representative images and quantification of TUNEL staining **(F)** Representative image and quantification of distribution of TUNEL staining in villus, transit amplifying (TA) zone, and crypt base. Unless otherwise noted, each data point is the mean of three representative sections per mouse with bar at median value and p denotes value of unpaired parametric Student's t test. Scale bar 100 µM. All data from distal small intestine of mice two days post final tamoxifen injection.

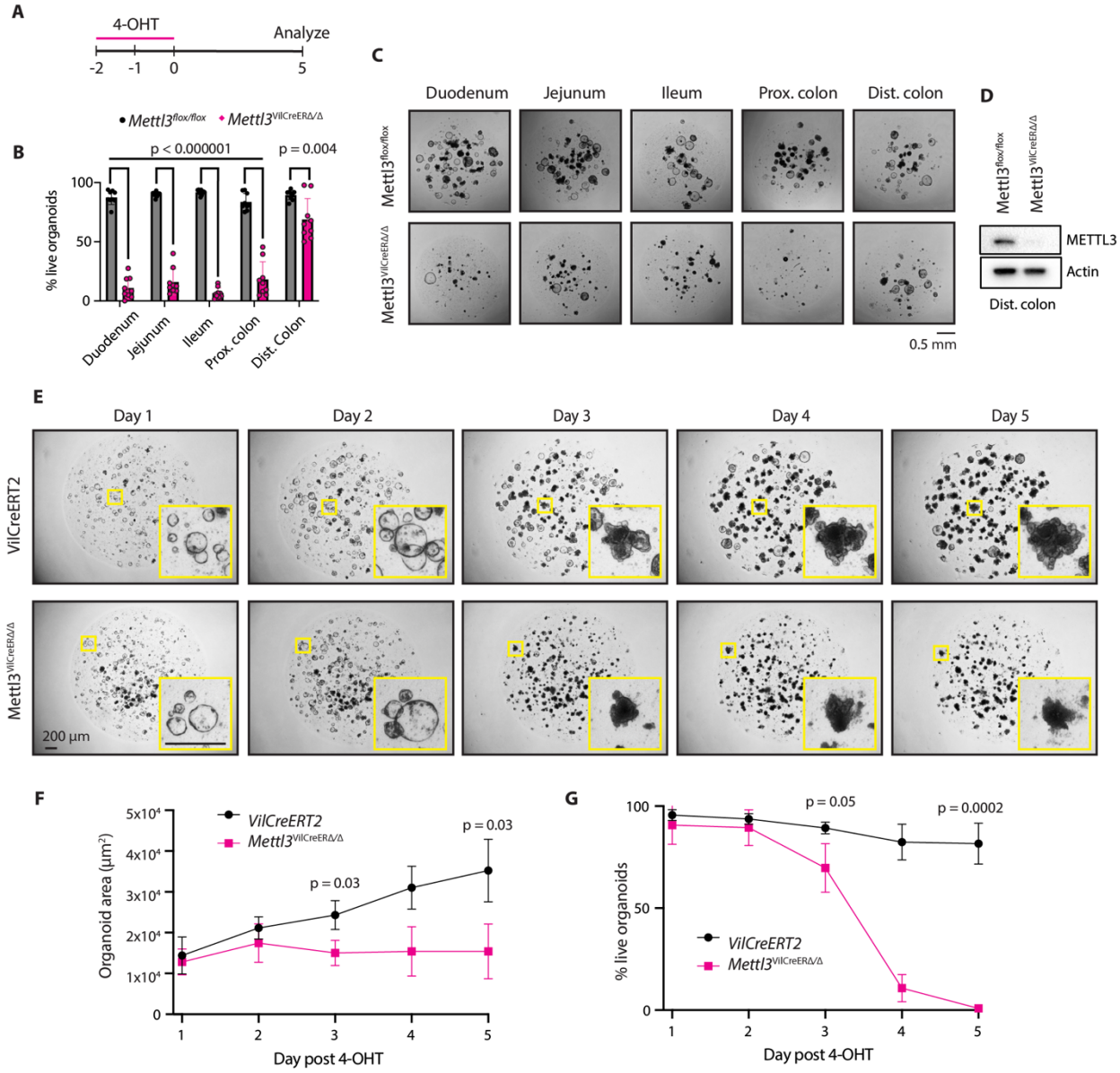

Figure 5. METTL3 deletion triggers growth arrest and death in intestinal epithelial enteroids and colonoids. (A) Intestinal epithelial enteroids or colonoids were treated with 1 µm 4-OHT 48 and 24 hours before beginning of time course and analyzed at days 1 through 5. **(B)** Percent live enteroids or colonoids from indicated tissue regions at 5 days post 4-OHT treatment. Each point represents n=9 technical replicates across n=3 passage separated biological replicates per genotype. Bar height at median value with error bars as +/- SD. **(C)** Representative images at 5 days post 4-OHT treatment corresponding to quantification in (B). **(D)** Western blot for METTL3 in surviving *Mettl3*$^{VilCreER\Delta/\Delta}$ distal colonoids six days after 4-OHT treatment. **(E)** Representative images of ileal enteroids in the five days post 4-OHT treatment. **(F, G)** ImageJ quantification of average ileal enteroid 2D area and percent live enteroids in the five days post 4-OHT treatment of *Villin-CreERT2* (VilCreERT2) and *Mettl3*$^{VilCreER\Delta/\Delta}$ enteroids. N=3 passage separated replicates. Data presented as mean +/- SD. P-value represents unpaired parametric Student's t test at day 3 and day 5.

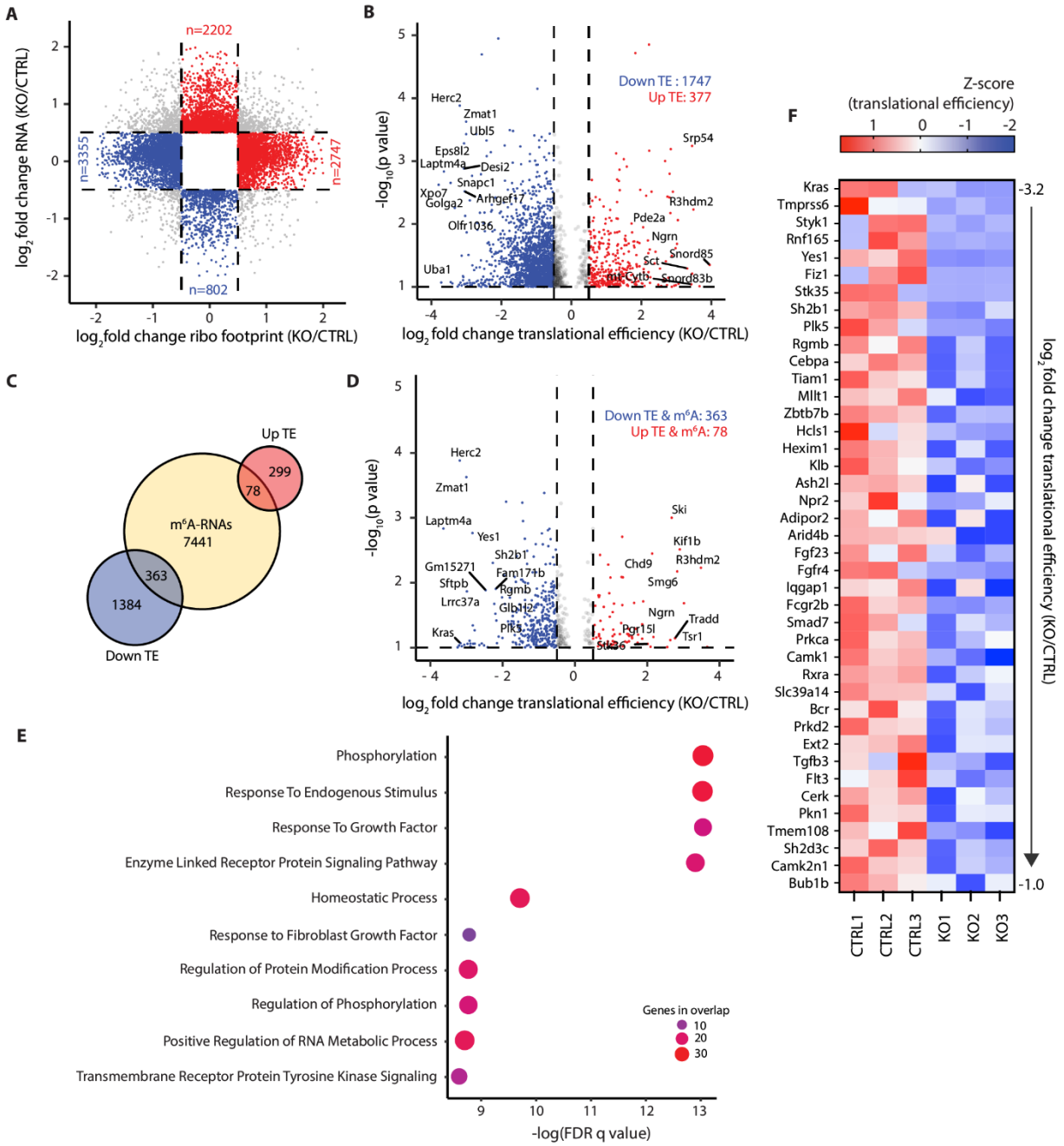

Figure 6. METTL3 deletion leads to a global decrease in mRNA translational efficiency with impacts on growth factor signaling. (A) Scatter plot of $\log_2$ fold change in ribosome footprint and total transcript abundance for all transcripts detected in RNA-seq and Ribo-seq of *Mettl3*$^{flox/flox}$ (CTRL) and *Mettl3*$^{VilCreER\Delta/\Delta}$ (KO) ileal enteroids 72 hours post initiation of 4-OHT treatment. Log2 fold change cut off >0.5 or <-0.5. Red marks transcripts increased in RNA or ribosome footprint abundance only. Blue marks decreases in RNA or ribosome footprint abundance only. Grey marks transcripts changed in both. **(B)** Volcano plot of all transcripts with $\log_2$ fold change in translational efficiency (TE) >0.5 or <-0.5 and $-\log_{10}$ p value >1. Red marks all transcripts with increased TE and blue marks all transcripts with decreased TE. **(C)** Venn diagram depicting fraction of transcripts with changes in TE and at least one m^{6}A peak as determined by m^{6}A-seq of wildtype mouse small intestinal crypt epithelium. Yellow circle is all m^{6}A-methylated transcripts detected by m^{6}A-seq. Blue circle is all transcripts with decreased TE from (B). Red circle is all transcripts with increased TE from (B). **(D)** Volcano plot of all transcripts displayed in (B), now filtered for transcripts

881 containing at least one m^6A peak. **(E)** Pathway enrichment analysis comparing transcripts with
882 downregulated TE ($log_2FC < -1$) and at least one m^6A peak against Gene Ontology Biological Process
883 (GOBP) gene sets. Circle color and size both scale with number of genes overlapping between the tested
884 gene set and the GOBP gene set. **(F)** Heat map depicting Z-scores for TE in three *Mettl3*$^{flox/flox}$ (CTRL) and
885 three *Mettl3*$^{VilCreER\Delta/\Delta}$ (KO) replicates 72 hours post initiation of 4-OHT treatment. Genes presented are all
886 42 genes from the four most significantly enriched pathways in (E). Genes are presented in order of greatest
887 decrease in mean TE to smallest. All data from RNA-seq and Ribo-seq of *Mettl3*$^{flox/flox}$ (CTRL) and
888 *Mettl3*$^{VilCreER\Delta/\Delta}$ (KO) ileal enteroids 72 hours post initiation of 4-OHT treatment.
889

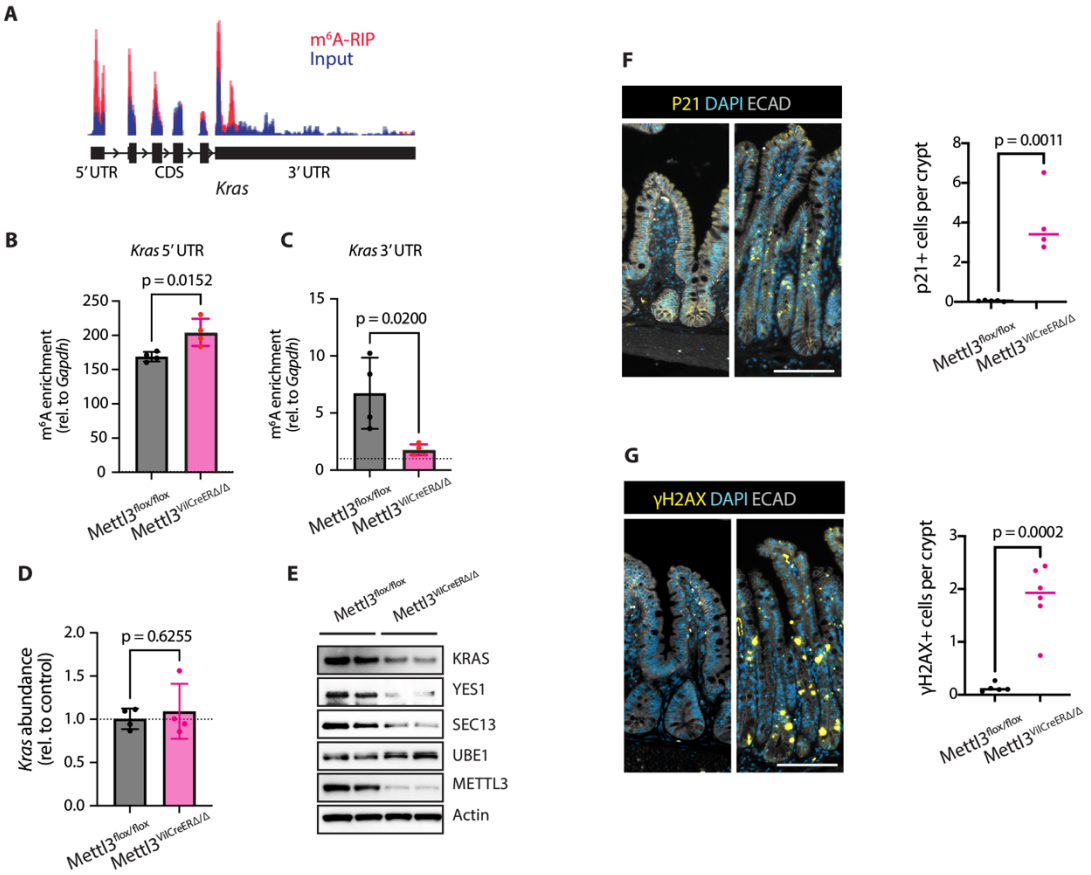

Figure 7. METTL3 deletion downregulates KRAS and induces cellular senescence. (A) Integrated Genomics Viewer depiction of read density for m^{6}A-RIP (red) and input RNA (blue) for the *Kras* transcript as determined by m^{6}A-seq in distal small intestinal crypts of n=3 wildtype mice. **(B, C)** m^{6}A-enrichment determined by m^{6}A-RIP-qPCR with primers targeting *Kras* 5' and 3' UTR in crypt enriched lysates from *Mettl3$^{flox/flox}$* and *Mettl3$^{VilCreERΔ/Δ}$* mice 3 days post-tamoxifen (n=2M, 2F per genotype). The m^{6}A enrichment score is the result of dividing the ratio of the target-of-interest in RIP compared to RIP input by the ratio of *Gapdh* (negative control) in RIP compared to RIP input. Data presented as median +/- SD. P-value represents unpaired parametric Student's t test. **(D)** qPCR for *Kras* transcript in crypt enriched lysates from *Mettl3$^{flox/flox}$* and *Mettl3$^{VilCreERΔ/Δ}$* mice 3 days post-tamoxifen (n= 2M, 2F per genotype). Data normalized to *Actb* and the mean of *Mettl3$^{flox/flox}$* controls. Data presented as median +/- SD. P-value represents unpaired parametric Student's t test. **(E)** Western blot for top targets with downregulated TE in crypts of *Mettl3$^{flox/flox}$* and *Mettl3$^{VilCreERΔ/Δ}$* mice two days post final tamoxifen injection (n=2 mice per genotype). **(F, G)** Representative images and quantification of p21 and γH2AX staining in distal half small intestine of *Mettl3$^{flox/flox}$* and *Mettl3$^{VilCreERΔ/Δ}$* mice two days post final tamoxifen injection. Images and quantification from areas of most severe histological distortion in distal small intestine of mice two days post final tamoxifen injection. Each data point is the mean of three representative sections imaged per mouse with bar at median value and p denotes value of unpaired parametric Student's t test. Scale bar 100 μM.

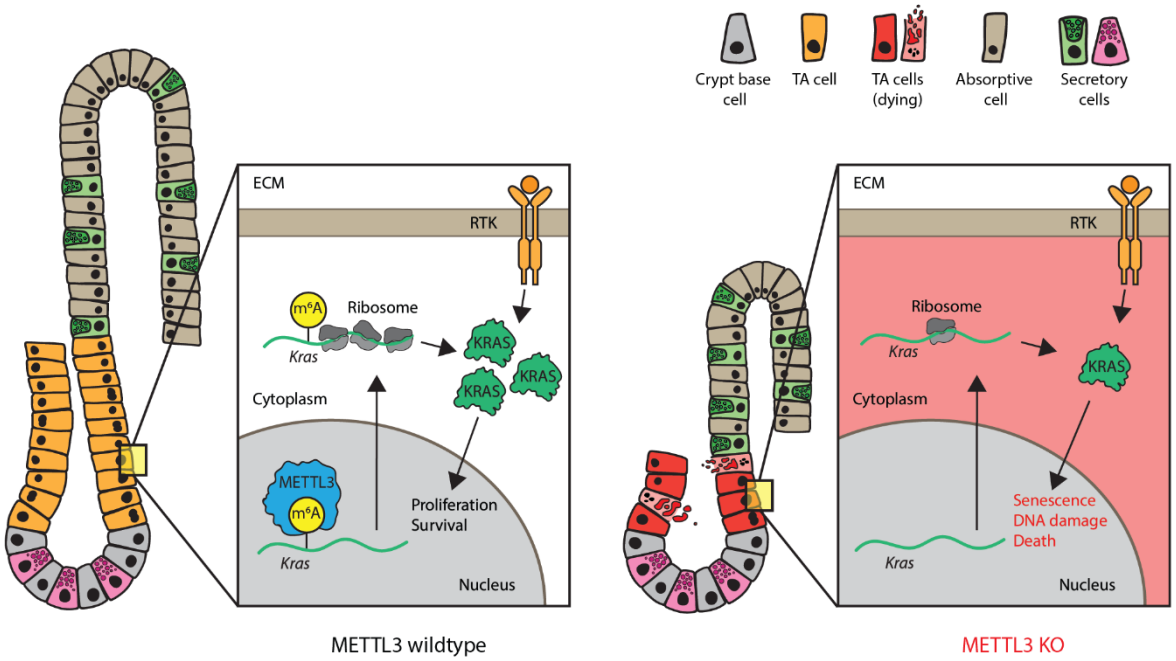

Figure 8. METTL3 maintains growth factor signaling and survival in intestinal transit amplifying cells. Proposed model. METTL3 methylates *Kras* and other transcripts involved in transducing growth factor signaling. Methylation promotes translation of these transcripts, enhancing proliferation and survival in transit amplifying (TA) cells downstream of external growth factors. In the absence of METTL3, a decreased response to extracellular growth factors in METTL3 knockout TA cells leads to cellular senescence and death. Loss of transit amplification results in reduced crypt and villus size and diminished production of absorptive cells. ECM, extra cellular matrix. RTK, receptor tyrosine kinase.

Supplementary Materials for

Intestinal transit amplifying cells require METTL3 for growth factor signaling, KRAS expression, and cell survival

Charles H. Danan et al.

*Corresponding author. Email: hamiltonk1@chop.edu

This PDF file includes:

Supplemental Figures 1-5
Supplemental Tables 1-3

Other Supplementary Materials for this manuscript include the following:
Supplemental Data 1-2

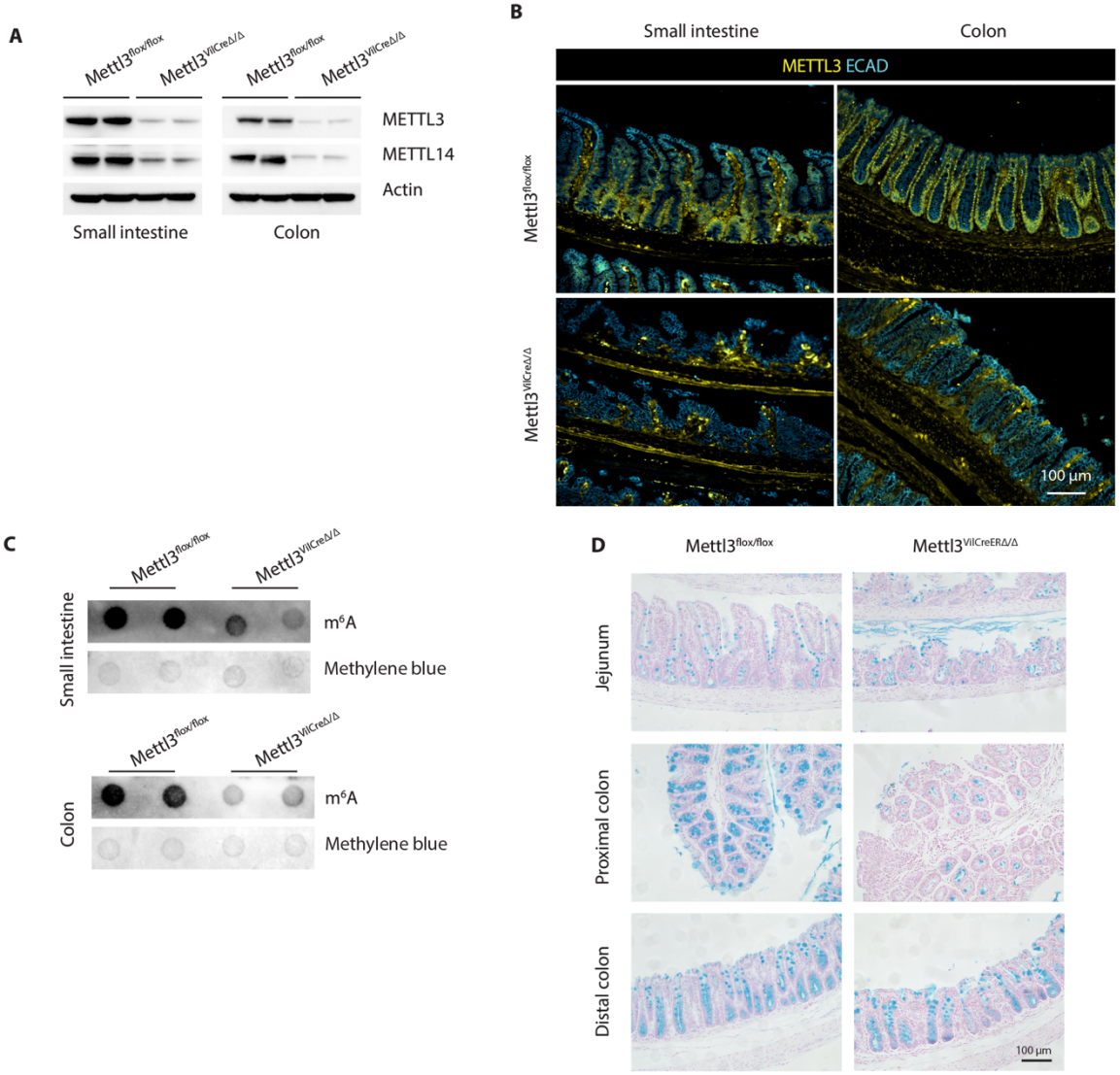

Supplemental Figure 1. Verification and additional intestinal phenotypes in *Mettl3$^{VilCre\Delta/\Delta}$* mice. (A) Western blot for METTL3 and METTL14 in epithelial crypt enriched lysates from distal half of small intestine and colon. **(B)** Immunofluorescent staining of METTL3 in jejunum. **(C)** m^{6}A dot blot in isolated crypts of distal half of small intestine and colon. **(D)** Representative Alcian blue staining in small intestine and colon. All data from postnatal day 29.

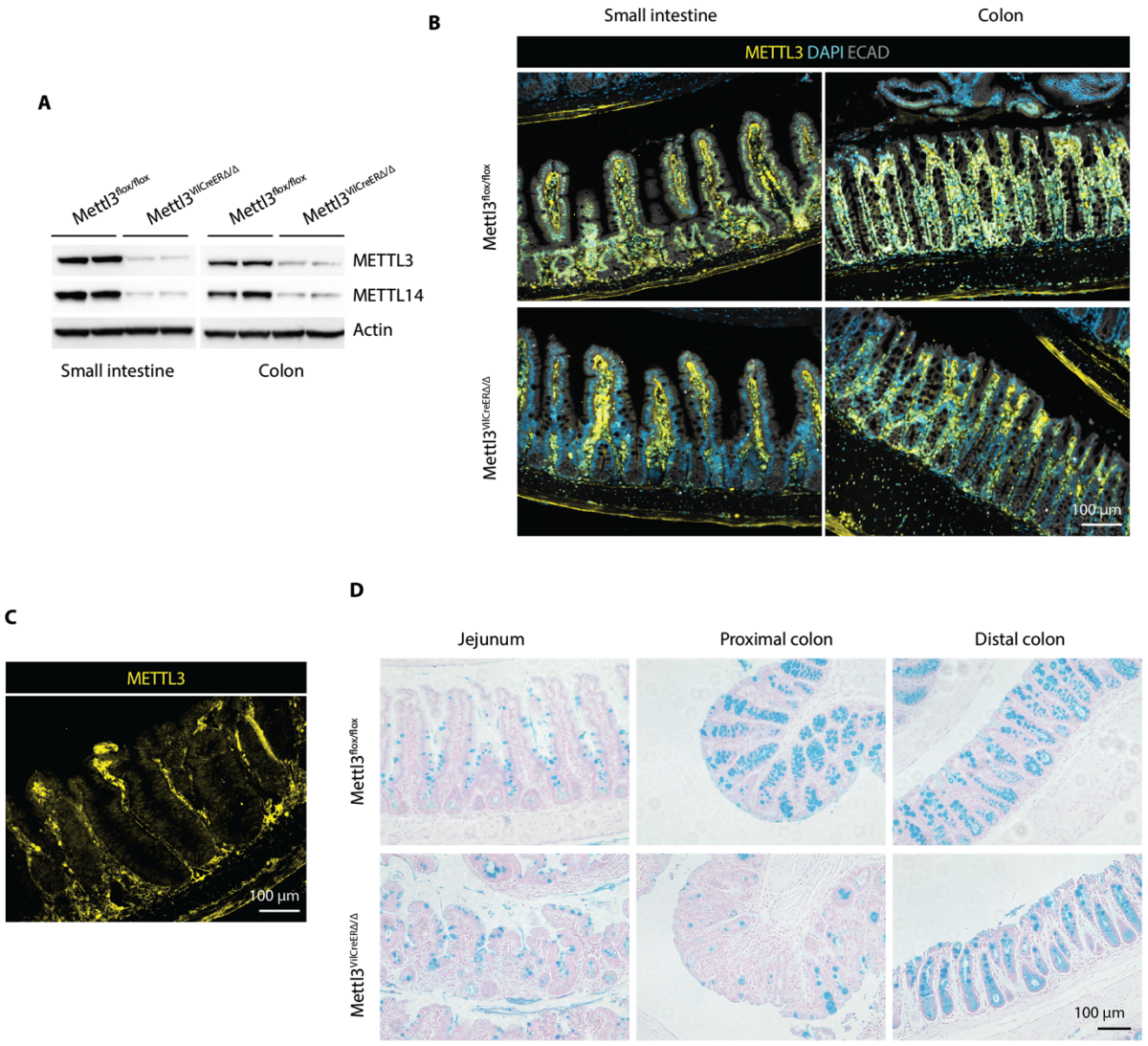

Supplemental Figure 2. Validation and additional characterization of inducible *Mettl3*$^{VilCreER\Delta/\Delta}$ mice. **(A)** Western blot for METTL3 and METTL14 in epithelial crypt enriched lysates from distal half of small intestine and colon in mice two days post final tamoxifen injection. **(B)** Immunofluorescent staining of METTL3 in jejunum and colon two days post final tamoxifen injection. **(C)** METTL3 staining in hypertrophic small intestinal crypts in a *Mettl3*$^{VilCreER\Delta/\Delta}$ mouse nine days post final tamoxifen injection. **(D)** Representative Alcian blue staining nine days post final tamoxifen injection.

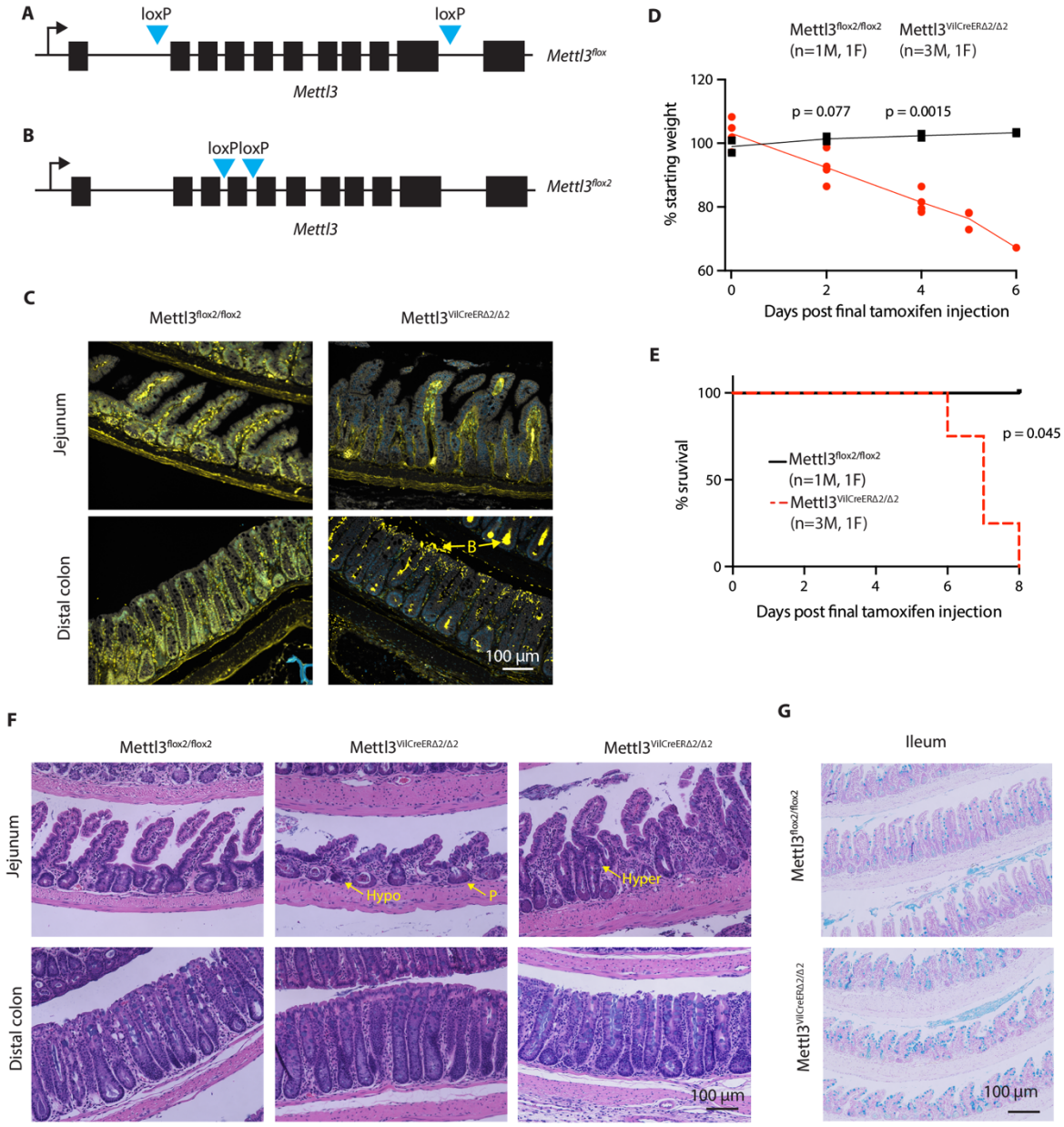

Supplemental Figure 3. A second *Mettl3* deletion model recapitulates intestinal phenotypes. (A, B) Schematic depicting *loxP* sites in the *Mettl3* gene. **(C)** METTL3 staining in jejunum and distal colon. "B" indicates presumed off-target luminal bacterial staining with anti-METTL3 antibody. **(D)** Weight loss post final tamoxifen injection in *Mettl3*$^{flox2/flox2}$ (n=2) and *Mettl3*$^{VilCreERΔ2/Δ2}$ (n=4) mice. Each individual point represents one mouse. **(E)** Kaplain-Meier survival curve post final tamoxifen injection in *Mettl3*$^{flox2/flox2}$ (n=2) and *Mettl3*$^{VilCreERΔ2/Δ2}$ (n=4) mice. **(F)** Representative H&E images from small intestine and colon. "Hypo" indicates hypoplastic crypts. "Hyper" indicates hyperplastic crypts. "P" indicates crypts dominated by Paneth cell granules. **(G)** Representative Alcian blue staining of ileum. Images from areas of most severe histological distortion in distal small intestine of mice meeting euthanasia criteria or littermate, tamoxifen-injected controls.

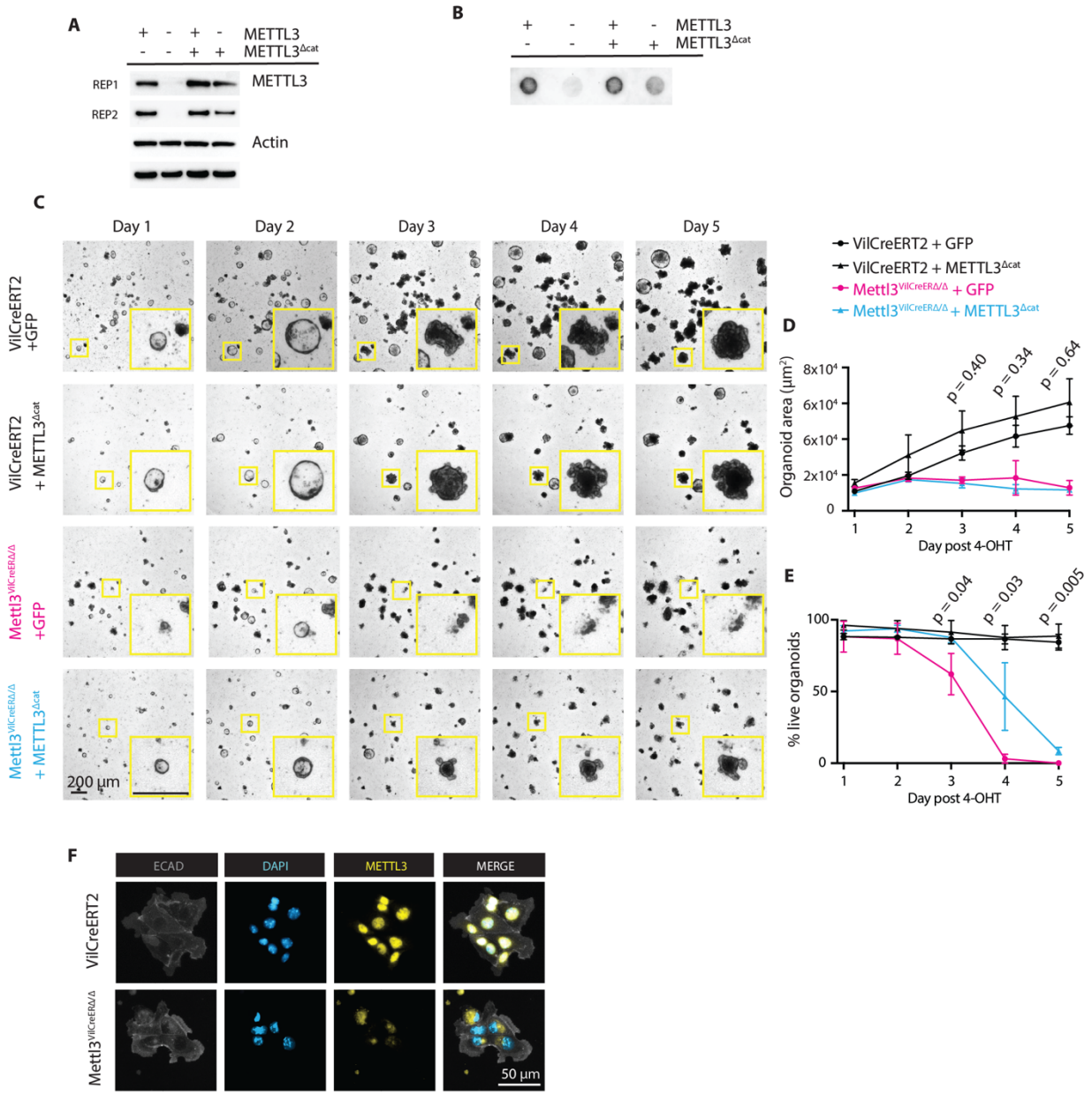

Supplemental Figure 4. Catalytic inactive METTL3 does not rescue death of *Mettl3*$^{VilCreERΔ/Δ}$ enteroids. (A) Western for METTL3 two days post 4-OHT. **(B)** m^{6}A dot blot in enteroids three days post 4-OHT. Each dot is 35 ng isolated mRNA. **(C)** Representative images of enteroid appearancein the five days post 4-OHT treatment. Individual enteroids are highlighted in yellow insets. **(D)** ImageJ quantification of average enteroid 2D area at each day post 4-OHT treatment from (C). Each point represents n=3 passage-separated biological replicates. Data presented as mean +/- SD. **(E)** Percent live enteroids at each day post 4-OHT treatment in enteroids from (C). Each point represents n=3 passage-separated biological replicates. Data presented as mean +/- SD. For D & E, P-value represents unpaired parametric Student's t test on days 3, 4, 5. P-values shown are for the comparison between *Mettl3*$^{VilCreERΔ/Δ}$ + GFP vs *Mettl3*$^{VilCreERΔ/Δ}$ + METTL3^{Δcat}. **(F)** Whole mount staining of METTL3 in intestinal epithelial monolayers two days post 4-OHT treatment.

983

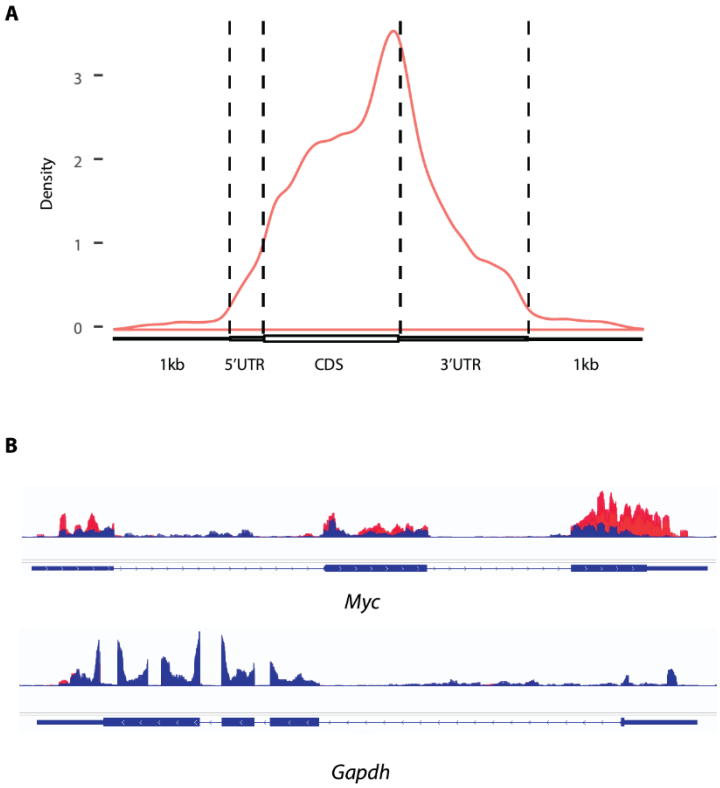

Supplemental Figure 5. Quality control for m^{6}A-seq. (A) Metagene density plot depicting distribution of m^{6}A peaks called by Exomepeak2 within m^{6}A-seq data from wildtype mouse small intestinal crypt epithelium. **(B)** m^{6}A-seq read density (red) compared to input RNA read density (blue) for positive control (*Myc)* and negative control (*Gapdh*) transcripts as seen in Integrated Genomics Viewer.

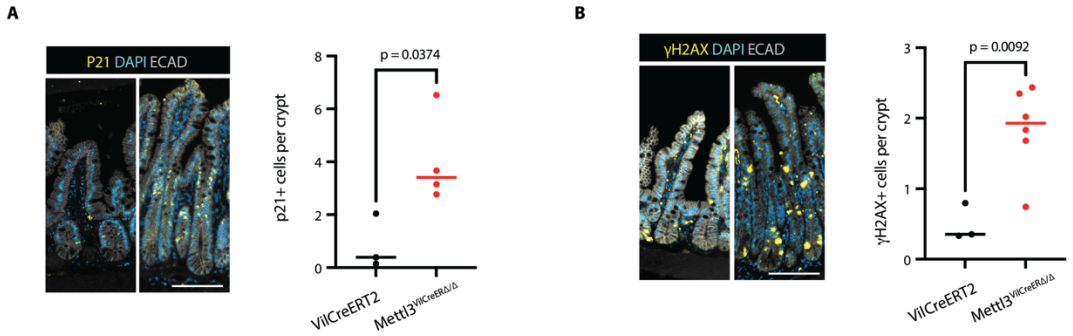

991
992 **Supplemental Figure 6. Increases in senescence and genomic instability after METTL3 deletion are**
993 **significant compared to *Villin-CreERT2* controls. (A and B)** Representative images and quantification
994 of p21 (n=3,4) and γH2AX (n=3, 6) staining in distal half small intestine of *Villin-CreERT2* and
995 *Mettl3*$^{VilCreERΔ/Δ}$ mice two days post final tamoxifen injection. Images and quantification from areas of most
996 severe histological distortion in distal small intestine of mice two days post final tamoxifen injection. Each
997 data point is the mean of three representative sections imaged per mouse with bar at median value and p
998 denotes value of unpaired parametric Student's t test. Scale bars 100 μM.
999

1000

Primary antibody- IF	**Catalog number**	**Antigen retrieval condition (if applicable)**
Rabbit anti-METTL3	abcam ab195352	Tris-EDTA pH 9.0
Rabbit anti-p21	Proteintech 28248-1-AP	Tris-EDTA pH 9.0
Rabbit anti-Phosphorylated-Histone H2A.X (Ser139)	CST 9718	Tris-EDTA pH 9.0
Rabbit anti-SP-1 Chromogranin A	Immunostar 20085	Tris-EDTA pH 9.0
Rabbit anti-LYZ1	Dako A0099	Citric Acid pH 6.0
Rabbit anti-MUC2	Genetex GTX100664	Citric Acid pH 6.0
Rabbit anti-Ki67	abcam ab16667	Citric Acid pH 6.0
Goat anti-E-Cadherin	R&D Systems AF748	Either antigen retrieval method
Mouse anti-beta-Actin	Sigma A5316	
Rabbit anti-METTL14	Sigma HPA038002	
Rabbit anti-UBE1	Proteintech 15912-1-AP	
Rabbit anti-SEC13	Proteintech 15397-1-AP	
Mouse anti-c-Yes	Santa Cruz sc-8403	
Rabbit anti-KRAS	Proteintech 12063-1-AP	
Secondary antibody- IF		
Alexa Fluor 488 Anti-goat IgG	Jackson 805-545-180	
Cy3 Anti-Rabbit IgG	Jackson 711-165-152	
Secondary antibody- Western		
Anti-rabbit HRP	CST 7074	
Anti-mouse HRP	Novus NBP1-75249	

1001

1002 **Supplemental Table 1.** Full list of primary and secondary antibodies used in this study.

1003

Feature graded	Grade	Description
Inflammation	0	None
	1	Slight
	2	Moderate
	3	Severe
Extent	0	None
	1	Mucosa
	2	Mucosa and submucosa
	3	Transmural
Regeneration	4	No tissue repair
	3	Surface epithelium not intact
	2	Regeneration with crypt depletion
	1	Almost complete regeneration
	0	Complete regeneration or normal tissue
Crypt damage	0	None
	1	Basal 1/3 damaged
	2	Basal 2/3 damaged
	3	Only surface epithelium intact
	4	Entire crypt and epithelium lost
Villus damage (SI only)	0	No change in villus height
	1	25% reduction in villus height
	2	50% reduction in villus height
	3	75% reduction in villus height
	4	Complete loss of villus
Percent involvement	1	1-25%
	2	26-50%
	3	51-75%
	4	76-100%

1004

1005 **Supplemental Table 2.** Histopathological scoring rubric adapted from (55) used for small intestine and
1006 colonic histopathological scoring, with scoring rules added for villus damage (villus damage only
1007 assessed in small intestine).
1008

Gene	Assay number
Actb	Mm02619580_g1
Olfm4	Mm01320260_m1
Bmi1	Mm03053308_g1
Clu	Mm01197002_m1
Lgr5	Mm00438890_m1
Ascl2	Mm01268891_g1
Cd44	Mm01277161_m1
Hopx	Mm00558630_m1
Kras 3' UTR (also used for total transcript)	Mm00517494_m1
Kras 5' UTR	Mm00517491_m1
Gapdh	Mm99999915_g1

1009
1010 **Supplemental Table 3.** Full list of Taqman qPCR primers used in this study.
1011
1012
1013

1014 **Supplemental Data 1. (separate file). RNA-seq and Ribo-seq in METTL3 KO**
1015 **enteroids.**
1016 Full results of RNA-seq and Ribo-seq from n=3 *Villin-CreERT2* (CTRL) and n=3
1017 *Mettl3*$^{VilCreER\Delta/\Delta}$ (KO) enteroid biological replicates 72 hours after initiating 4-OHT
1018 treatment. Green columns and blue columns display transcripts per million (TPM)
1019 values output by Kallisto in total RNA and ribosome footprint RNA fractions,
1020 respectively. Light orange columns correspond to translational efficiency (TE) values for
1021 each transcript determined by dividing the TPM in the total RNA library by the TPM in
1022 the ribosome footprint library for each individual transcript and sample. P value refers to
1023 the comparison between mean TE of CTRL vs mean TE of KO replicates.
1024
1025
1026 **Supplemental Data 2. (separate file). m6A-seq in wildtype mouse crypt epithelium.**
1027 Full output of exomePeak2 analysis of m^{6}A-sequencing data produced in epithelial cells
1028 sorted from distal small intestinal crypts of n=3 adult wildtype mice.
1029